FUNDAMENTAL EXPERIMENTAL TESTS AND MODELING OF LOX/CH4 ENGINES AT HIGH PRESSURES

by

JESSICA BLUE BAKER
B.S. University of Central Florida, 2020
M.S. University of Central Florida, 2022

A dissertation submitted in partial fulfillment of the requirements
for the degree of Doctor of Philosophy
in the Department of Mechanical and Aerospace Engineering
in the College of Engineering and Computer Science
at the University of Central Florida
Orlando, Florida

Summer Term
2024

Major Professor: Subith S. Vasu

ABSTRACT

In recent years, the space travel industry has grown exponentially, resulting in the need for a low-cost, efficient rocket engine fuel. As such, there has been renewed interest in utilizing liquid natural gas (LNG) as it is less likely to soot than kerosene-based fuels and has widespread availability and low cost of use as compared to the traditional RP-X and even liquid methane (LCH_4) fuels due to the reduced need for refinement. However, current literature does not fully cover varying blends of natural gas and the effects that impurities have on natural gas/methane fuels, with most studies being confined to low-pressure applications. Therefore, new experimental ignition delay time measurements at rocket engine relevant pressures are essential to ensure current chemical kinetic models capture the ignition behavior at these elevated conditions and to determine the optimal purity levels for a reliable, cost-efficient, aerospace-grade LCH_4/LNG fuel. The current work explores various blends of natural gas/methane fuel with various impurities, including higher hydrocarbons as well as nitrogen-carriers. A shock tube study was carried out to study the ignition delay times and carbon monoxide time histories of these natural gas blends utilizing chemiluminescence and laser absorption spectroscopy at 20, 50 and 100 atm over temperatures ranging from 1400-1700 K and at an equivalence ratio of 1. The experimental data was then compared to two different chemical kinetic mechanisms: the industry-standard GRI 3.0 and the in-house UCF 2022. The data is used to improve chemical kinetic mechanisms and modeling of LNG fuels for rocket engine applications.

to my friends and family: it has been quite a wild ride

ACKNOWLEDGMENTS

I would like to acknowledge my advisor Dr. Subith Vasu for his understanding, support, and commitment to my growth throughout my degree. Thank you to my committee members Dr. Michael Kinzel, Dr. Jayanta Kapat, and Dr. Darren Tinker for their time and willingness to be on my committee.

Thank you to the members of ER13 at NASA MSFC that made my stay so memorable and especially to Dr. Darren Tinker who offered his time, mentorship, and understanding throughout the marathon that is grad school. I learned so much more than I could have imagined during my time as a NASA fellow and sometimes I still can't believe I got the opportunity at all. Thank you to the members of DLR-VT in Stuttgart for their expertise and especially to Dr. Clemens Naumann and Dr. Marina Braun-Unkhoff for being so knowledgeable and helpful. Thank you to Dr. Seetha Raghavan for selecting me for the NSF IRES program as the experience shaped me, both professionally and personally, more than I can say. Thank you to my colleagues and friends at the lab and especially to Dr. Andrew Laich and Dr. Ramees K. Rahman, whose guidance and discussions were invaluable. This work would not have been possible without their support and candor.

Thank you to my friends for traveling with me and being totally awesome and to my family for their constant love, support, and advice. I absolutely would not have been able to complete this program without them. And thank you to those that sponsored this effort: the National Air and Space Administration (grant number 80NSSC21K2056), the Department of Energy (DE-FE0032072), the NASA Florida Space Grant Consortium, and the University of Central Florida.

As my time in graduate school comes to an end, I offer a bittersweet thank you to both the University of Central Florida and to the city of Orlando for hosting me during the best and worst times of my life. In the words of Peter Lewis Kingston Wentz III, “thanks for the memories….”

TABLE OF CONTENTS

LIST OF FIGURES

LIST OF TABLES

CHAPTER ONE: INTRODUCTION

Background

Space travel is currently experiencing growth at its fastest pace in years as the commercial space industry matures, reaching a record value of $546 billion in 2022 with a projected annual revenue of one trillion dollars by 2040 [1]. While much of the growth has been generated by the commercial sector, there are considerable increases in government spending on both military and civil space programs in the United States. With such rapid growth underway, liquid methane (LCH_4) and liquid natural gas (LNG) have gained popularity as a rocket fuel with the U.S. Department of Defense (DoD) and NASA because engines using these fuels are considered more reliable for multiple launches and such fuels are far less likely to soot than kerosene-based fuels. Also, commercially available CH_4 has widespread availability and low cost compared to RP-x liquid aerospace fuels. However, there are stringent impurity standards implemented for rocket applications, as impurities may affect the ignition and chemical kinetic properties of aerospace-grade LCH_4. As such, it is necessary to determine the optimal impurity level for these fuels by experimentally investigating methane fuel blends with varying impurities.

Liquid natural gas used in aerospace engines is a highly refined form of pipeline natural gas, however, refinement is a process that often incurs significant costs and will still result in the final LCH_4 blend having extraneous species such as nitrogen and higher hydrocarbons at ppm levels [2]. Even at these ppm levels, the trace species can have chemically and thermally significant concentrations that may cause shifts in combustion characteristics. Therefore, to reduce the uncertainty introduced from these impurities, a highly refined and pure form of liquid methane is commonly used as a fuel during the design stage. For practical applications, the DOD has developed impurity guidelines for LCH_4 fuels. Thus, to promote space access, it is essential to determine the optimal purity levels while complying with government standards for a reliable, cost-efficient, aerospace-grade LCH_4/LNG fuel. A selection of the Department of Defense's breakdown of the grading standards used for LCH_4 can be seen in Table 1.

Table 1: Performance Specification of LCH_4 as a Propellant[3]

Property	**Grade**		
	A	**B**	**C**
Purity (CH_4), % Vol, min	98.7	99.9	99.97
Water, ppmV, max	1	0.5	0.5
Oxygen, ppmV, max	1	1	1
Nitrogen, ppmV, max	5000	100	100
Carbon dioxide, ppmV, max	125	50	50
Other gaseous impurities, ppmV, max (i.e. Ar, H_2, He, Ne)	5000	125	125
Ethane (C_2H_6), ppmV, max	5000	500	100
Propane (C_3H_8), ppmV, max	3000	500	100
Other volatile hydrocarbons, ppmV, max	1	1	1
Total volatile sulfur, ppmV, max	1	0.1	0.1
Non-volatile residue (NVR) & particulates, mg/L, max	10	1	1

In order for the suitability of these impurity standards to be validated, an investigation into the ignition properties of these LCH_4 and other CH_4-based fuels is needed. Since N_2 and N_2-based species are known diluents in pipeline natural gas and appear in proportionally larger percentages of the LCH_4 DoD graded blends, this study will also include N2 as an impurity in select natural gas mixtures. Different blends of natural gas will be studied in a shock tube to represent various time steps in the pipeline natural gas refinement process (varying levels of the higher hydrocarbon species, including ethane, propane, butane, nitrogen).

While the composition of pipeline natural gas can vary based on location and vendor, a breakdown of a selected composition of pipeline natural gas is presented in Table 2 as a comparison.

Table 2: Composition of Pipeline Natural Gas [4]

Species	Purity CH_4	C_2H_6	C_{3+} alkanes	N_2	CO_2	O_2	H_2	CH_3SH & Sulfur Species
Conc.	94.9 % vol	25,000 ppm	2,900 ppm	16,000 ppm	7,000 ppm	200 ppm	trace	2.7 ppm

In addition to the study of various mixtures of natural gas and methane-based fuels, larger scale hot fire testing (with an average chamber pressure of 46 atm) will be carried out to provide additional validation targets and give a wholistic approach to improvement of rocket combustor analysis and modeling. CH* is closely related to combustion reactions and is often used as an indicator that ignition is occurring. The distribution of CH*/chemiluminescent images during hot fire testing gives important information about the combustion process including the presence/location of vigorous chemical reactions, information about the combustion stability, and can be used to reflect flame structure.

Imaging also presents further validation targets as it can be compared to CFD simulations which will then allow for further refinement of the mechanism used, resulting in improved models for canonical rocket combustor flow analysis. This, with a modeling software used by NASA and DOD agencies called Two Dimensional Kinetics (TDK), will allow for direct comparison of chemical kinetic mechanism performance with outputs such as Isp [5, 6].

The overall objective of this work is to gain a better understanding of the behavior of methane-based fuels at conditions relevant to rocket engines (pressures up to 500 atm and temperatures from 1000 to 3000 K) as current models lack relevant data and have yet to be validated experimentally. Combining different modes of investigation such as lower technology-readiness-level shock tube experiments and TDK studies with higher level analyses such as CFD simulations and CH* imaging during hot fire testing will allow for refinement of the chemical kinetic mechanisms resulting in improved models for canonical rocket combustor flow analysis and a comprehensive data set.

Literature Review

Though there have been past efforts to understand the ignition characteristics of natural gas blends with varying levels of impurities, many studies focus on CO_2 addition and are targeted at gas turbine applications. While there are a multitude of neat natural gas studies available in the literature, data is often confined to lower pressures (less than 50 atm) and such studies do not necessarily discuss different natural gas blends, rather focusing on one natural gas blend as compared to neat methane.

There is currently a gap in the literature for the study of fuels at pressures relevant to rocket engine applications and ppm levels of impurities that may appear in such fuels. Further studies at higher pressures and varying levels of impurity would be beneficial to furthering the knowledge of the ignition of such natural gas fuels and are essential to ensure current chemical kinetic models capture the ignition behavior at these elevated conditions.

Natural Gas Mixtures

There is significant literature available on ignition characteristics of neat methane fuels, but most studies focus on lower pressures with applications towards gas turbines or gas engines [7-10]. Some natural gas mixtures have been covered in the literature, though data is often confined to lower pressures (less than 50 atm), well outside of the applications for rocket engines [11-15]. For example, a study carried out by Shao utilized methane/ethane/propane blends of natural gas, but carried out experiments at pressures near 12 atm [16]. Some shock tube-focused literature covers higher pressures, such as a study done by Karimi et al. that looked at methane autoignition at pressures up to 200 atm, though this study featured very high CO2 dilution [17]. Other works at higher pressures include past studies carried out by Petersen et al., that were able to obtain ignition delay times via pressure measurement techniques at up to 480 atm [18-20].

Other studies featuring natural gas blends tend to be focused on different applications and, while some do discuss emissions, these studies focus more heavily on different applications or strategies, including the effects of injection timing and fueling strategies with varying applications (such as supercritical CO2/pilot ignited engines) [21-23]. One such study carried out by Li looked at a wider pressure range up to 300 atm, but with applications towards injection strategies and nozzle parameters, not necessarily discussing ignition parameters [24]. Additionally, Naber studied a single natural gas mixture featuring methane/ethane/propane/butane and nitrogen, but carried out experiments in a combustion vessel targeting conditions relating to diesel engines [25].

Many investigations into natural gas can be found that utilize either very high purity methane or such large percentages of diluents (such as ethane/propane) in the fuel composition that they are well beyond the DOD impurity level guidelines which would be representative of a raw/pipeline natural gas mixture [24, 26-29]. One shock tube study investigated ignition delay times at pressures up to 30 atm, but had large percentages of ethane and propane (10-20%), far surpassing what would be seen in crude natural gas [30].

There are studies that do specifically look at the effects of higher-hydrocarbons on methane purity, but they tend to focus on one specific additive/impurity as opposed to modeling or recreating a natural gas blend that may be commercially available [21, 31, 32]. A study carried out by Lifshitz focused on the influence of propane on methane oxidation reactions in a shock tube, but utilized solely methane and propane, not including other higher hydrocarbons found in pipeline natural gas [33]. Additionally, Scheller investigated methane-oxygen mixtures with various amounts of ethane and propane as additives, but, again, utilized the additives individually, not necessarily representing the composition of an aerospace-grade LNG blend [34].

There are few studies that directly compare different natural gas blends to assess purity standards. A study carried out by Vallabhuni did investigate two different LNG mixtures in a shock tube, but focused on lower-purity methane blends and lower pressures (up to 40 atm) for applications relating to gas engines [35]. Crane also investigated methane/ethane/propane/butane natural gas mixtures, but focused more on simulations with experimental measurements limited to a single blend and pressures at sub-atmospheric conditions [36]. Finally, Mehta carried out natural gas experiments in a shock tube at pressures up to 240 atm, but did not include ignition data (such as ignition delay times), while Sahu investigated three different natural gas blends, but compared an aerospace-grade comparable blend to that of a methane purity much lower than the nominal crude natural gas blends (62.5% CH_4) thereby limiting understanding of the effects of small amounts of diluents on the methane purity [37, 38]. These studies represent the limited scope of work done to compare various natural gas blends and their ignition properties and performance. Additional work is needed in order to properly understand the behavior of natural gas fuels and the effects of purification at conditions relevant to rocket engine applications.

Methane/Natural Gas+N_2O

More generally, there are some past studies featuring methane or natural gas blends with nitrogen-carriers added as an impurity/diluent. For example, a study done by Grillo featured shock tube experiments with neat methane and nitrogen addition, but at much higher nitrogen composition than that found in crude natural gas [39]. There are also studies focused on NH3 or other nitrogen-carrier addition to natural gas fuels, but these studies largely focus on applications for power generation and are carried out at lower pressures [40-43].

There are few studies in the high pressure range that utilize N_2O as an impurity/additive to natural gas. Also, N_2O is often found in literature combined with natural gas/methane at much higher percentages than ppm levels. For example, a shock tube study by Deng et al. studied N_2O oxidation with methane and did report ignition delay times, but was done at pressures up to only 16 atm [44]. Similarly, other studies with high percentages of N_2O (or N_2O utilized as an oxidizer) also appear in the literature, once again at pressures well below rocket engine applications [45-47]. There are two particularly relevant studies that focus on ppm levels of N_2O addition. One study by Rahman et al. presents ignition delay time data from a shock tube study of natural gas+CO_2 with 500 ppm impurity of N_2O at 100 atm pressure condition [48]. This study, along with a shock tube ignition delay time investigation of CH_4/N_2O oxidation done by Mathieu et al., represent the limited scope of past work done on ppm levels of N_2O impurity (though the Mathieu study covered a minimum of ~800 ppm of N_2O at pressures up to 28 atm) [49]. Further studies at higher pressures and varying levels of N_2O impurity would be beneficial to furthering the knowledge of the ignition of such natural gas fuels.

Imaging

Additionally, there have been some past chemiluminescence studies of nozzles, but few exist at rocket engine relevant pressures ranges or observe OH*, with most imaging studies investigating general flame chemiluminescence or IR features over a broader wavelength [50-52], solid fuel rockets [53-55], or studying more compact setups on smaller magnitudes (such as the BEM-1/BEM-2 plumes) [56, 57]. The studies that do observe CH* are on smaller scale combustors. For example, a study done by Hu recorded CH* distribution but was carried out via spontaneous radiation imaging in a reverse-flow combustor at an inlet pressure of 1 atm [58]. Another study carried out by Jens recorded OH* chemiluminescence but with applications for solid fuels and pressures up to 15 atm, while An investigated flame chemiluminescence in a rocket-based combined cycle combustor at pressures up to 26 atm [50, 54]. There are various imaging studies carried out in rotating detonation engines, but these studies focus on detonation characteristics and are again at lower pressures [59, 60]. One such study carried out by Rankin used OH* chemiluminescence imaging of an RDE, but RDEs are optically accessible devices and offer support for more straight-forward chemiluminescence imaging, something that is not always possible during hot fire tests. These studies represent the limited literature available on chemiluminescence studies for rocket engine plumes and related applications. Further investigation and data would be beneficial to furthering the state of knowledge and providing future validation targets for various simulations and mechanism improvements.

CHAPTER TWO: METHODOLOGY

Shock Tube Facilities

Shock tubes are nearly ideal devices for studying gas-phase high-temperature combustion phenomena as the entire heating process occurs on a microsecond time-scale with the system holding pressure and temperature throughout the test time and experiments having high reproducibility. The following facilities both feature high-purity, stainless steel shock tubes with an internally electropolished finish to reduce wall friction, and thus mitigate the ability of the boundary layer formation.

Kinetics Shock Tube Facility

Experiments carried out at the 2 and 20 atm pressure ranges utilized the University of Central Florida's (UCF) lower pressure, kinetics shock tube facility. The kinetics shock tube is a high-purity, stainless steel shock tube facility with an inner diameter of 14.17 cm. The shock tube is divided into two sections: the driven and the driver which are separated by a thin Lexan diaphragm. The driven section is vacuumed down to less than 5E-5 torr before each experiment and is then filled with the mixture of interest. The driver is filled with an inert gas such as helium, and, when the pressure of the inert gas reaches the necessary amount, the diaphragm ruptures and propagates a normal shock wave down the length of the tube.

The velocity of the incident shock wave was measured using five piezoelectric pressure transducers (PCB 113B26; 500 kHz frequency response) equally spaced along the last 1.4 m of the shock tube linked to four time-interval counters (Agilent53220A; 0.1 ns time resolution) which are then channeled through a logarithmic amplifier. An RTV-coated Kistler pressure transducer (Kistler 603B1-piezoelectric) is used to obtain pressure traces during ignition while limiting thermal effects.

These incident shock velocity values were then linearly extrapolated to obtain the reflected shock velocity at the end wall location. The pressure and temperature after the reflected shock wave were calculated based on the extrapolated velocity, initial pressure, initial temperature, and normal 1-D shock relations. The test section consists of eight equally-spaced optical ports located 2 cm from the end wall, with one port being equipped with a pressure transducer (Kistler 603B1-piezoelectric). All measurements using the kinetics shock tube were taken at this 2 cm location. More information about the facility can be found in earlier publications and a diagram of the shock tube can be seen in Figure 1.

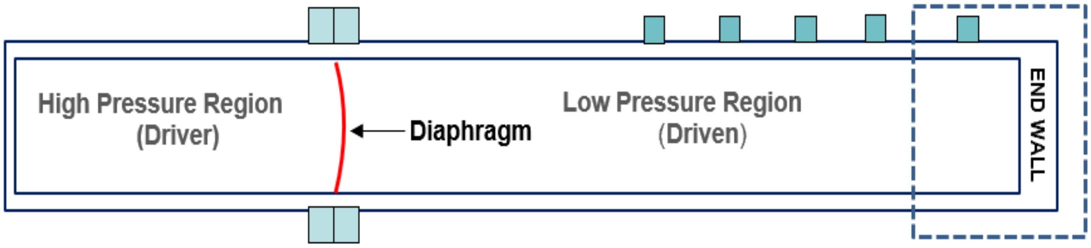

Figure 1: Schematic of the UCF kinetics shock tube

Mixture Preparation

Test mixtures were made in the 33-liter, stainless steel, chemically inert mixing tank. The kinetics shock tube's mixing tank is fitted with a magnetically driven stirrer to ensure homogeneity of the mixture. Mixtures were prepared manometrically, measuring the partial pressures with 100-Torr and 10,000 Torr baratrons and test mixtures were allowed to homogenize for 4+ hours before experiments were carried out. Research-grade quality gases were used to prepare the test mixtures and the mixing tank was vacuumed out to less than 0.10 torr between each mixture preparation.

Diagnostics

For the 2 and 20 atm measurements, ignition delay times (IDTs) were measured. IDTs can be determined in multiple different ways and, depending on the definition, can result in differences of more than 100 µs [49]. For this study, IDT is defined as the time between the arrival of the reflected shockwave to the time coinciding with the point of the maximum logarithmic emission signal. A representative pressure and emission profile can be seen in Figure 2. Ignition delay time measurements were via a photomultiplier tube (Model 2032) with a 310 ± 2 nm bandpass filter to isolate the OH* emission at the 2 cm location from the end wall.

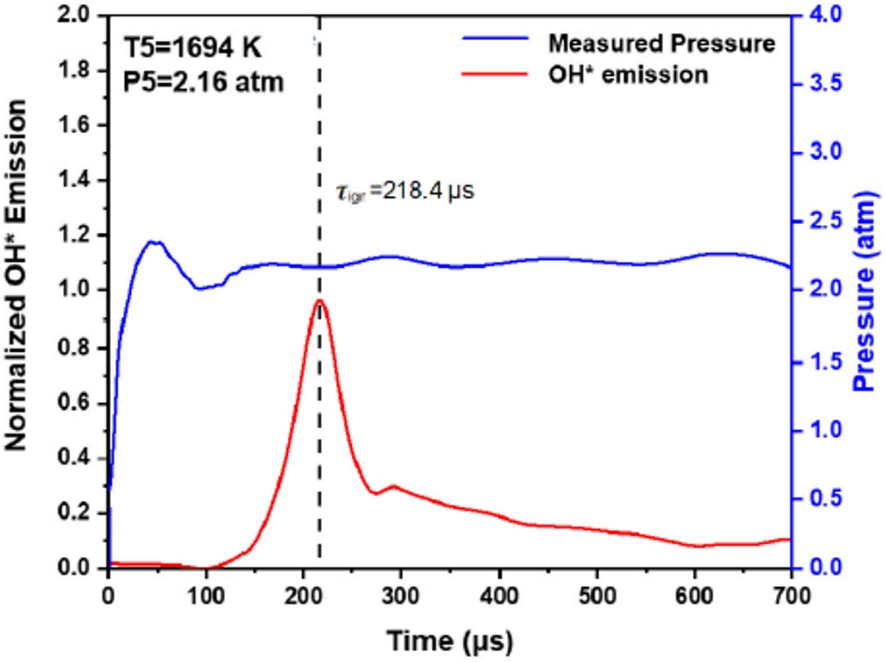

Figure 2: Pressure and normalized OH* emission trace during stoichiometric ignition of NG mixture in the 2 atm pressure range

Carbon monoxide time histories were also measured; these time histories measurements were taken at the 2 cm location utilizing fixed wavelength absorption spectroscopy with a distributed feedback quantum cascade laser (DFB QCL) targeting a CO absorbance peak at 2046.28 cm-1 where any potential interference from additional species was considered negligible. Data was recorded on a 500 MHz DAQ with 5 million samples and measurements were taken with the shock tube in vacuum, filled in the target mixture, and then during the experiment. For all of the 2 and 20 atm measurements, CO time histories were captured by aligning the laser through the shock tube. A schematic for the laser setup as well as an axial cross-section of the test section can be seen in Figure 3.

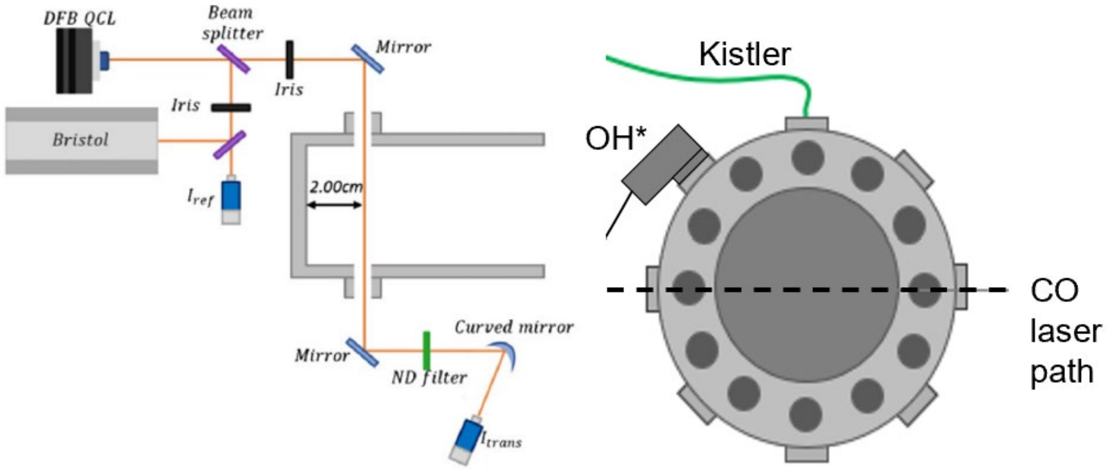

Figure 3: Schematic for the kinetics shock tube and laser diagnostic setup (left) and axial cross-section (right) for 2 and 20 atm experiments

The beam was first split via a 50/50 beam splitter which directed half of the beam into a reference detector (Vigo PVI-2TE-5.0) that allows for monitoring of power fluctuations in the laser during experiments. The other 50% of the beam was directed through a neutral density (1.0) filter which reduces extraneous emissions and ensures the output is purely CO. The beam then passes through the shock tube's sapphire windows and is captured by the transmitted detector. The spectral output was periodically monitored via a Bristol Spectrum Analyzer to ensure stability of the system. The experimental mole fractions were obtained via the Beer-Lambert Law and absorbance equation given in Equations (1) and (2), respectively.

$$X_{CO} = \frac{\alpha_v RT}{\sigma PL} \tag{1}$$

$$\alpha_v = -\ln\left(\frac{I}{I_o}\right)_v \tag{2}$$

Where α_v is the absorbance at frequency ν; R (J/mol-K) is the universal gas constant; T (K) is the temperature of the gas; σ (m2/molecule) is the absorption cross-section of the absorbing species; P (Pa) is the pressure of the gas; L (m) is the path length of the shock tube; and in Equation (2), I and I_o are the measured intensities of laser power in test gas mixture and in vacuum, respectively, at frequency ν. The absorption cross section values for these measurements were obtained from HITRAN 2016 database at each P5 and T5 condition where absorbance from potential interfering species was negligible [61].

The overall uncertainty in the IDT measurements is less than ±10%, resulting from uncertainty in mixture composition and reflected shock temperatures. The uncertainty for the CO mole fraction is estimated via a time-varying root mean square quantity where the uncertainties from the parameters of Beer's Law (Equation 1) are taken into account (parameters include pressure, temperature, absorbance, and absorption cross-section). More information about this method can be found in Ninnemann et al. [62].

HiPER-STAR Facility

Experiments carried out in the 50 and 100 atm pressure ranges utilized UCF's High Pressure, Extreme Range Shock Tube for Advanced Research (HiPER-STAR) facility. Functionally, the HiPER-STAR shock tube is very similar to the kinetics shock tube, so a broader overview focusing on the key differences will be highlighted here. The HiPER-STAR facility allows for high pressure combustion diagnostics relevant to rocket engine conditions. The shock tube has an inner diameter of 7.62 cm in the driven section and 12.7 cm in the driver section with a transition section featuring two area reductions on the fore and aft sections, creating a smooth transition from the larger driver to the smaller driven with a final 10.16 cm cross section.

HiPER-STAR's shock tube is also divided into two sections (driven and driver) which are now separated by an aluminum diaphragm located in the diaphragm housing assembly. For increased repeatability, the diaphragms are cut and scored in-house using a CNC-arc cutter and 3-axis mill, respectively. Aluminum diaphragms (6061-T6) with a thickness of 2.286 mm are used, with a corresponding fluoro-elastomer (Viton) spacer used to offset the gap and improve sealing. The diaphragms were scored to a depth of 0.635 mm to encourage uniform breaking and reliable test conditions. The driver is then filled with a combination of inert gases such as helium or mixtures of helium and nitrogen, in specific ratios (determined from previous experiments) to obtain the desired braking pressure.

Velocity of the initial shock is calculated in the same way, with five pressure transducers now equally spaced along the last 2 m of the tube with the post-reflected shock properties calculated based on the normal shock relations as discussed in the previous section. The test section consists of eight equally-spaced optical ports located 6 cm from the end wall, with one port again being equipped with an RTV-coated Kistler pressure transducer (Kistler 603CAA) to obtain pressure traces during ignition. More information about the facility can be found in earlier publications and a diagram of the shock tube can be seen in Figure 4.

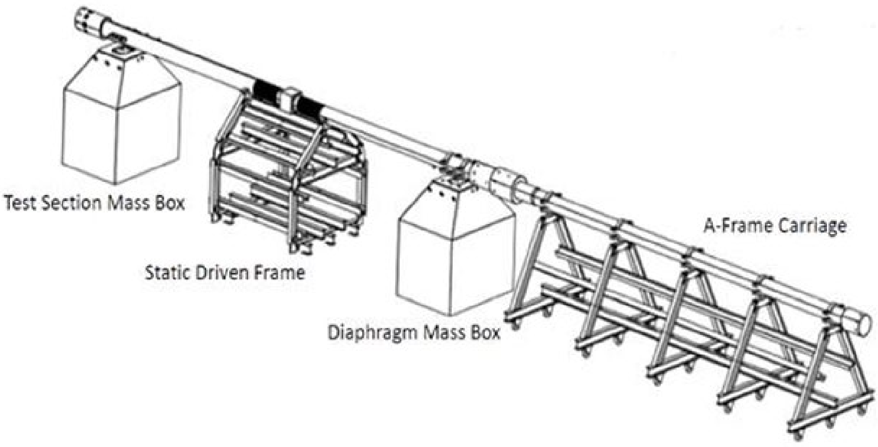

Figure 4: HiPER-STAR shock tube schematic [63]

Mixture Preparation

The mixtures prepared at this facility were made in a 60-liter mixing tank fitted with magnetic stirring paddles to ensure homogeneity of the mixture. Again, a manometric approach was utilized, measuring the partial pressures with 100 torr and 20,000 torr baratrons and utilizing research grade gasses to make the mixture. The mixing tank was vacuumed to sufficiently lower pressures between mixtures.

Diagnostics

For the 50 and 100 atm experiments, no CO time histories were measured, only ignition delay time measurements were obtained. The other ports of the test section are sealed with contoured plugs that house windows, allowing for emission detection through the test section. IDTs were calculated as described in the kinetics shock tube section, with a 310 nm bandpass filter to isolate the OH* as well as a 430 nm bandpass filter to isolate the CH* emission to provide a comparison for future measurements (where the OH* and CH* IDT peaks were within 3% of each other). A schematic for the axial cross section of the shock tube can be seen in Figure 5.

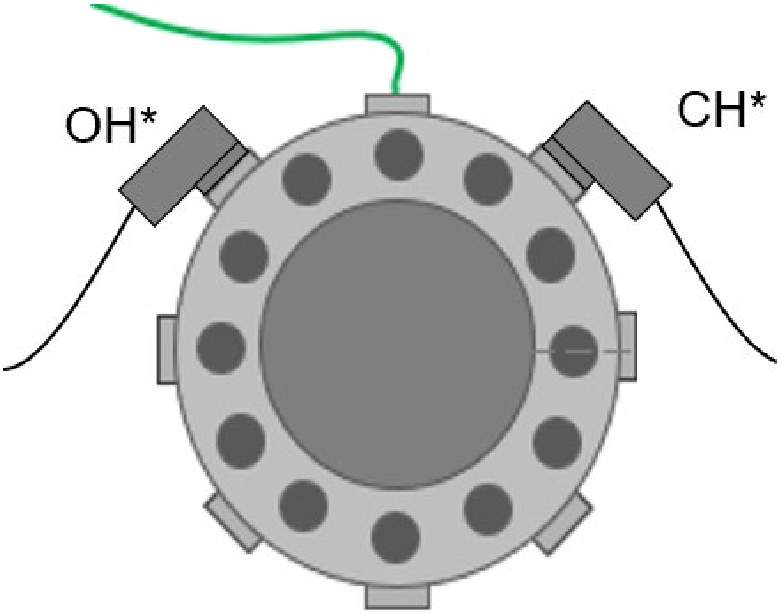

Figure 5: Axial cross section for 50 and 100 atm experiments

Data is collected using two NI PCIe-6376 Data 19 Acquisition Devices, with a sampling rate of up to 3.5 MHz per channel. The absorption cross section values were obtained from a previous study using methane-based fuels and is validated throughout the pressure and temperature range for the current study and can be seen in Figure 6 [64]. The resulting uncertainty in temperature and pressure lead to an average uncertainty of mixture IDT below 20%, which is a standard practice in the combustion community.

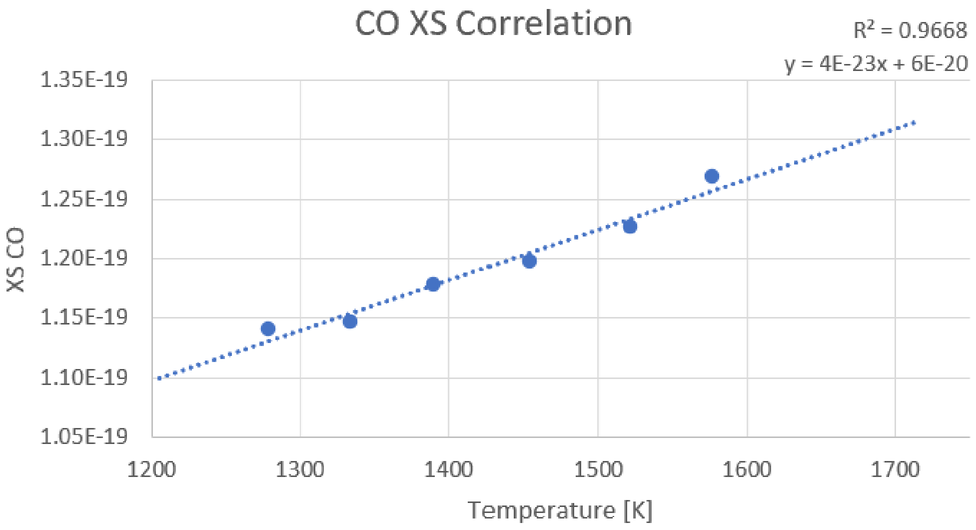

Figure 6: CO cross section correlation for high pressures

Hot Fire Test Stand Experimental Setup

Additionally, experiments run in collaboration with NASA Marshall Space Flight Center (MSFC) allow for unique opportunities to collect CH* chemiluminescent imaging data during hot fire testing. Combustion events occurring during hot fire testing of a lander class 7000-lbf thrust chamber using liquid oxygen (LOX)/LCH_4 propellants were recorded. Tests were performed at an average chamber pressure of 50 atm. Imaging was supporting the NASA RAMFIRE (Reactive Additive Manufacturing for Fourth Industrial Revolution) test series, focusing on hot fire testing of LOX/LCH_4 fuels in 3-D printed nozzles. More information about the test program and experimental details of the nozzle itself can be found in the literature by Tinker and Fedotowsky [65, 66].

Images were obtained using a high-speed camera (Photron Fastcam SA-Z), UV intensifier (Lambert HiCATT 25), and lens (Tamron 70-300 mm) with a 430 ± 5 nm bandpass filter to isolate the CH* emission, where most interfering species and effects of particles such as soot are outside the observable range and can be neglected. CO2* is one molecule that may have potential interference as it emits at the selected wavelength and can have greater intensity as compared to CH*. However, even with CO2* acting as a broad emitter, the intensity of the CH* signal can still be utilized to indicate intensity of the reaction and as an indicator of flame location under the assumption that CO2* production is proportional to CH* production. Additional information about this method can be found in the literature as described by Jens [54]. The sampling frequency was 2000 Hz and the intensifier gate width and camera frame rate were synced before each test to calibrate the system before image acquisition. Videos were obtained with a 1024x688 resolution. A schematic for the test stand setup can be seen in Figure 7, where the nozzle is located at the 'TS115 Cell' outlined in blue and the camera was setup in the 'Normal Video' zone outlined in red, located approximately 20 feet perpendicular from the nozzle.

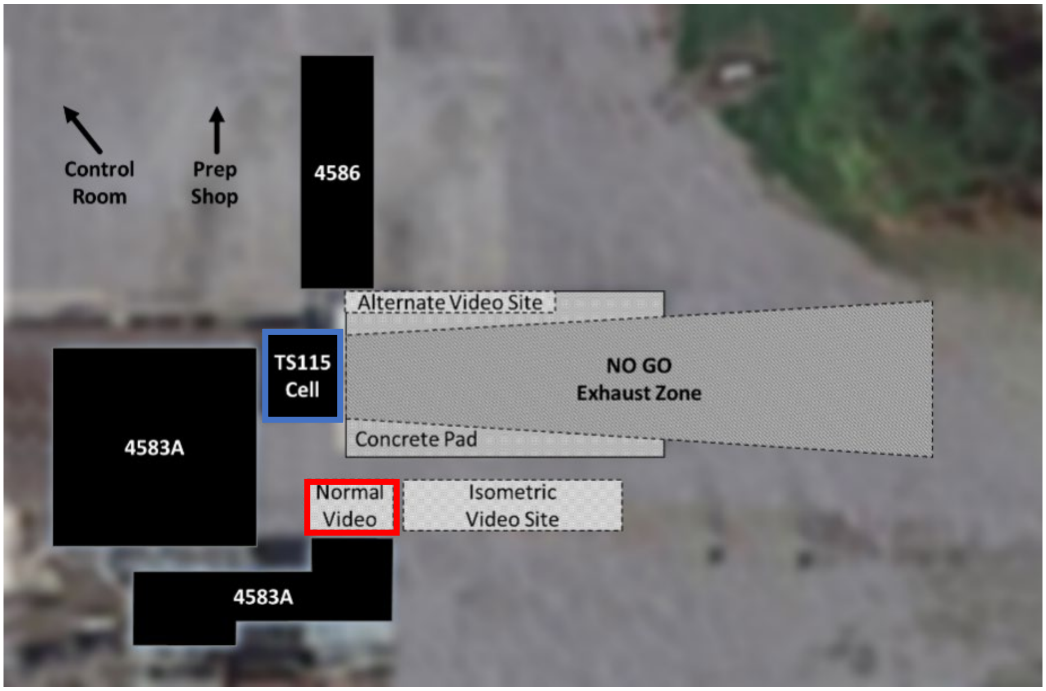

Figure 7: Aerial Schematic of MSFC Test Stand 115

CHAPTER THREE: MODELING

Chemical kinetic modeling will also be carried out to serve as a comparison and provide validation for the experimental data. A traditional 0-D CHEMKIN-Pro analysis is mostly used with the addition of 2-D TDK modeling to compare differences in Isp.

0-Dimensional Chemical Kinetic Modeling

Running preliminary simulations with initial estimates of how the species are expected to react under the tested environment assists in determining the range of experimental conditions that can be measured and the expected absorbance that the laser will detect. Initial simulations carried out at each relevant pressure (2, 20, 50, and 100 atm) and at the high and low end of each individual temperature range demonstrated that there will be negligible interference targeting the desired CO absorbance peak. Figure 8 shows a representative example of one such simulation, demonstrating that only CO will appear in the absorbance data.

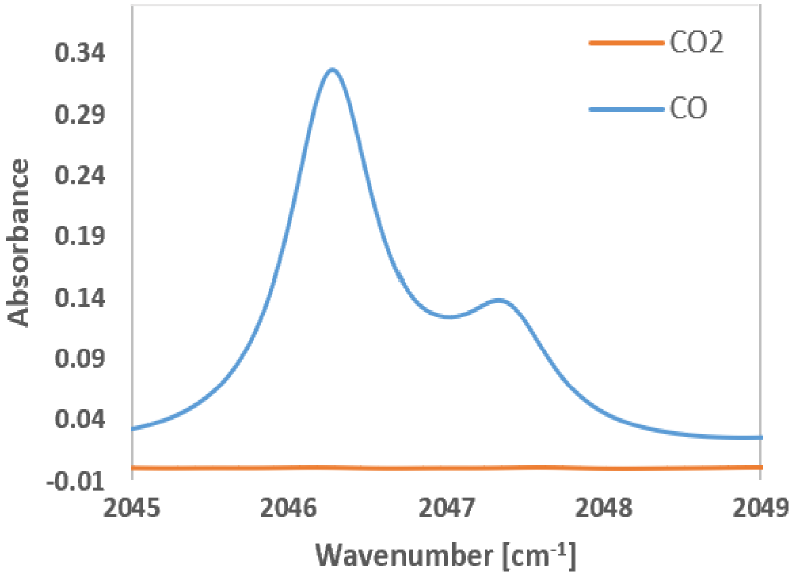

Figure 8: Preliminary CHEMKIN-Pro Simulation of UCF 2022 mechanism for Natural Gas Mixture 4 at 100 atm and 1500 K

Traditionally, numerical simulations of shock tube experiments are performed using ANSYS CHEMKIN-Pro with a closed, homogeneous (0-D) batch reactor under adiabatic conditions with constant UV assumption [67]. When the shock wave passes through the reaction mixture, the step change in temperature and pressure justifies the former assumption as both shock tubes are constant volume and any change in pressure would have been a result of boundary layer effects; both shock tubes have a large enough diameter compared to the boundary layer to minimize these effects. The adiabatic assumption can be justified as the whole process takes place on a millisecond time scale, minimizing heat transfer.

To simulate autoignition delay times and CO time histories for natural gas/methane mixtures, two different chemical kinetic mechanisms were used: UCF 2022 and GrI 3.0 [68, 69]. Within each of the mechanisms, there is information consisting of reaction rate equations of the gas-phase kinetics, thermodynamic properties, and transport properties for each reaction. The gas-phase kinetics file contains reaction rates/rate constant in the form of the Arrhenius equation (Equation 3), which is dependent on the molar activation energy for the reaction (E_a), the frequency or Arrhenius factor (A), temperature (T), and universal gas constant (R).

$$k = Ae^{-E_a/_{RT}} \tag{3}$$

The mechanism titled 'UCF 2022' was developed using a base mechanism from Rahman et al. that is proficient at predicting methane oxidation over a large pressure range[70]. The Rahman mechanism did not contain C_3 and C_4-hydrocarbon reactions, so it was combined with those higher hydrocarbon reactions from the Aramco 3.0 mechanism [71]. The UCF 2022 mechanism now consists of 121 species and 1040 reactions and was updated to include higher hydrocarbon reactions and various nitrogen-bath gas related reactions rates. This mechanism is well validated for ignition delay times of methane oxidation for pressures up to 300 atm. It is also validated with experimental data for oxidation of smaller hydrocarbons in the presence of nitrogen oxides. The two mechanisms used include the industry standard GRI 3.0

mechanism as well as the in-house mechanism, UCF 2022. Model results from CHEMKIN-Pro, including CO time histories and IDT measurements, are reported in the following sections as a comparison to the experimental results. A sensitivity analysis and reaction pathway analysis are also offered here (conducted with the UCF 2022 mechanism), and will be discussed in more detail in the following sections.

2-Dimensional Chemical Kinetic Modeling

In addition to the 0-D modeling, NASA's Two-Dimensional Kinetic code will also be used to validate predicted vs experimental Isp from hot fire tests. TDK gives performance parameters based on input geometry and a chemical kinetic mechanism, so it can be used to validate predicted versus experimental Isp from hot fire tests. This data could then potentially be used to predict Isp for various methane-blended fuels as well. TDK is the JANNAF standard for performance calculations as, unlike other ODE calculators, it includes kinetic losses in the nozzle which accounts for how long it takes for the chemistry to reach equilibrium. This will allow for a more robust chemical kinetic mechanism to be used in such modeling. TDK is highly useful for obtaining preliminary rocket engine performance parameters, but allows for only a maximum of 200 reactions, requiring a largely reduced mechanism. The UCF 2022 mechanism was heavily reduced in order to fit into the software and even further reduced to optimize software performance.

The various inputs/outputs from TDK are often limited distribution/ITAR restricted (including geometry of the nozzle, specific testing conditions, exact input mechanisms, and exact Isp values), so percent difference in Isp will be the only output offered to show dependence of the modeling software on mechanism robustness and provide a comparison between the JANNAF standard mechanism and the updated and reduced UCF 2022 mechanism.

CHAPTER FOUR: EXPERIMENTAL RESULTS

To provide a baseline validation for the in-house mechanism, Figure 9 demonstrates a past work done by the author utilizing one of the same neat natural gas (NG) mixtures (a 93% CH_4 purity mixtures) that is used throughout the low, intermediate, and high pressure ranges in the upcoming sections [72]. The experiments for this NG mixture (NG1, the specific composition of which will be discussed shortly) were performed in the same kinetics shock tube, using the same method, and at the same equivalence ratio (Φ= 1), but at a lower, standard pressure of 2 atm. This baseline model validation compares the UCF 2022 mechanism with the GRI 3.0 mechanism at a well-studied pressure range in order to further confirm basic model functionality. It can be seen that both of the mechanisms closely align with the experimental data (within the margin of error), which indicates good baseline agreement and functionality of the mechanisms.

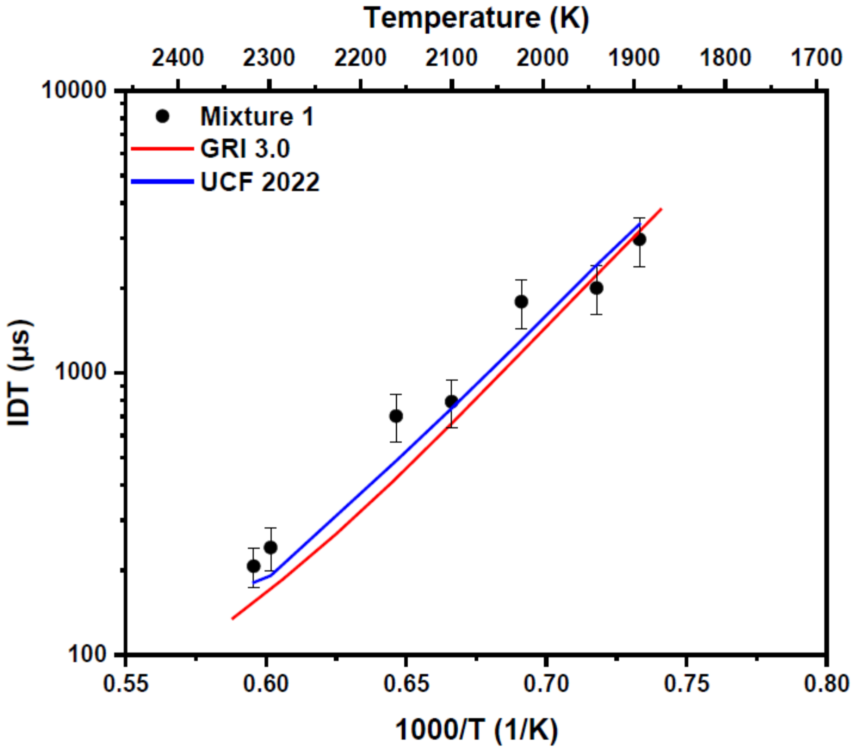

Figure 9: Comparison of shock tube IDTs during neat NG1 oxidation at 2 atm [68]

Low Pressure Natural Gas Blends

Various natural gas blends were experimentally studied in the UCF kinetics shock tube at an average pressure of 20 atm with temperatures ranging from 1400-1700 K at an equivalence ratio of 1. Table 3 shows the composition of the test mixtures used for this low pressure campaign (and note that test mixture NG4 is modeled after the Department of Defense's grade A LCH_4 fuel and NG2 is modelled after the sample pipeline natural gas composition from the EIA).

Table 3: Composition of Test Mixtures for Low Pressure Natural Gas Blends (by Percent Volume)

Test Mixtures	**Compound**					
	CH_4	**C_2H_6**	**C_3H_8**	**C_4H_{10}**	**N_2**	**N_2O**
NG1	93	4.75	1.5	0.75	0	-
NG1+N_2O	93	4.75	1.5	0.75	0	0.1%
NG2	94.9	2.5	0.3	0	2.3	-
NG2+N_2O	94.9	2.5	0.3	0	2.3	0.1%
NG3	96.04	3.96	0	0	0	-
NG3+N_2O	96.04	3.96	0	0	0	0.1%
NG4	98.7	0.5	0.3	0	0	-
NG4+N_2O	98.7	0.5	0.3	0	0	0.1%

Ignition Delay Times

Neat NG Mixtures

Shock tube ignition delay times of various blends of natural gas are offered as a comparison to observe the effect of methane purity on LNG fuels at 20 atm. The experimental data with best fit lines can be seen in Figure 10. As a baseline check, the obvious trend of elevated temperature resulting in quicker IDT for every mixture is confirmed. It was also found that, when comparing various blends of natural gas, higher CH_4 purity levels result in an increase in ignition delay time far outside of the margin of error. This indicates that the appearance of higher hydrocarbons such as ethane, propane, or butane have a significant impact on the ignition properties of natural gas blends, decreasing the ignition delay times.

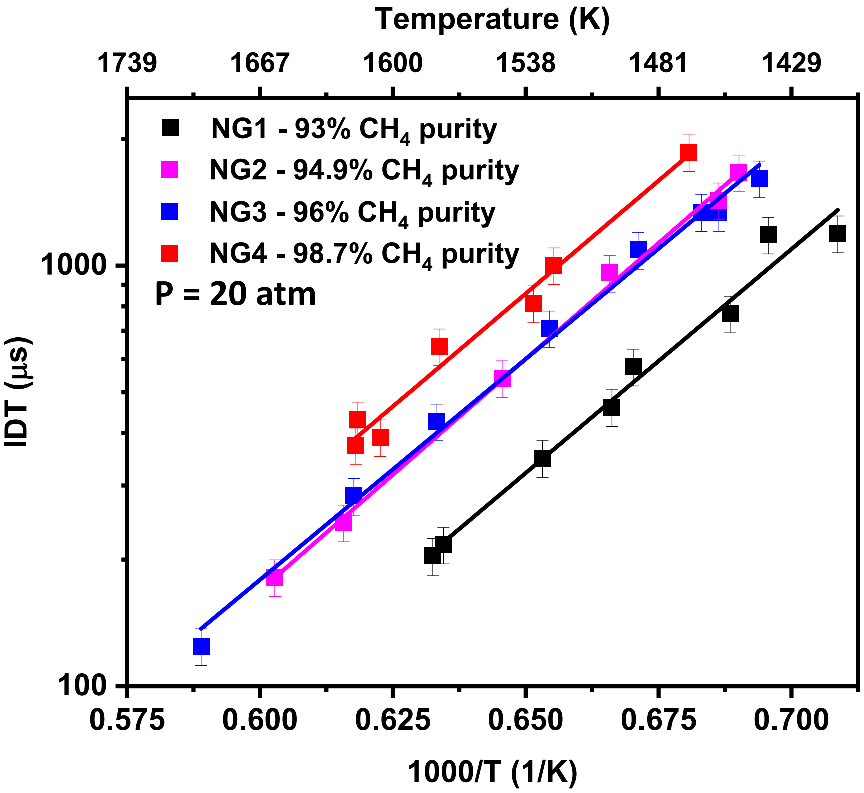

Figure 10: Comparison of shock tube IDTs during NG oxidation at 20 atm with best fit lines

Figure 11 shows the model comparison for all neat NG mixtures at 20 atm with the UCF 2022 mechanism shown in blue and the GRI 3.0 mechanism in red. It can be seen that the UCF 2022 mechanism is largely able to capture the experimental behavior of each mixture within the margin of error. The GRI 3.0 mechanism tends to underpredict the IDT, with larger variation at lower temperature conditions, indicating the importance of temperature on the mechanism's behavior.

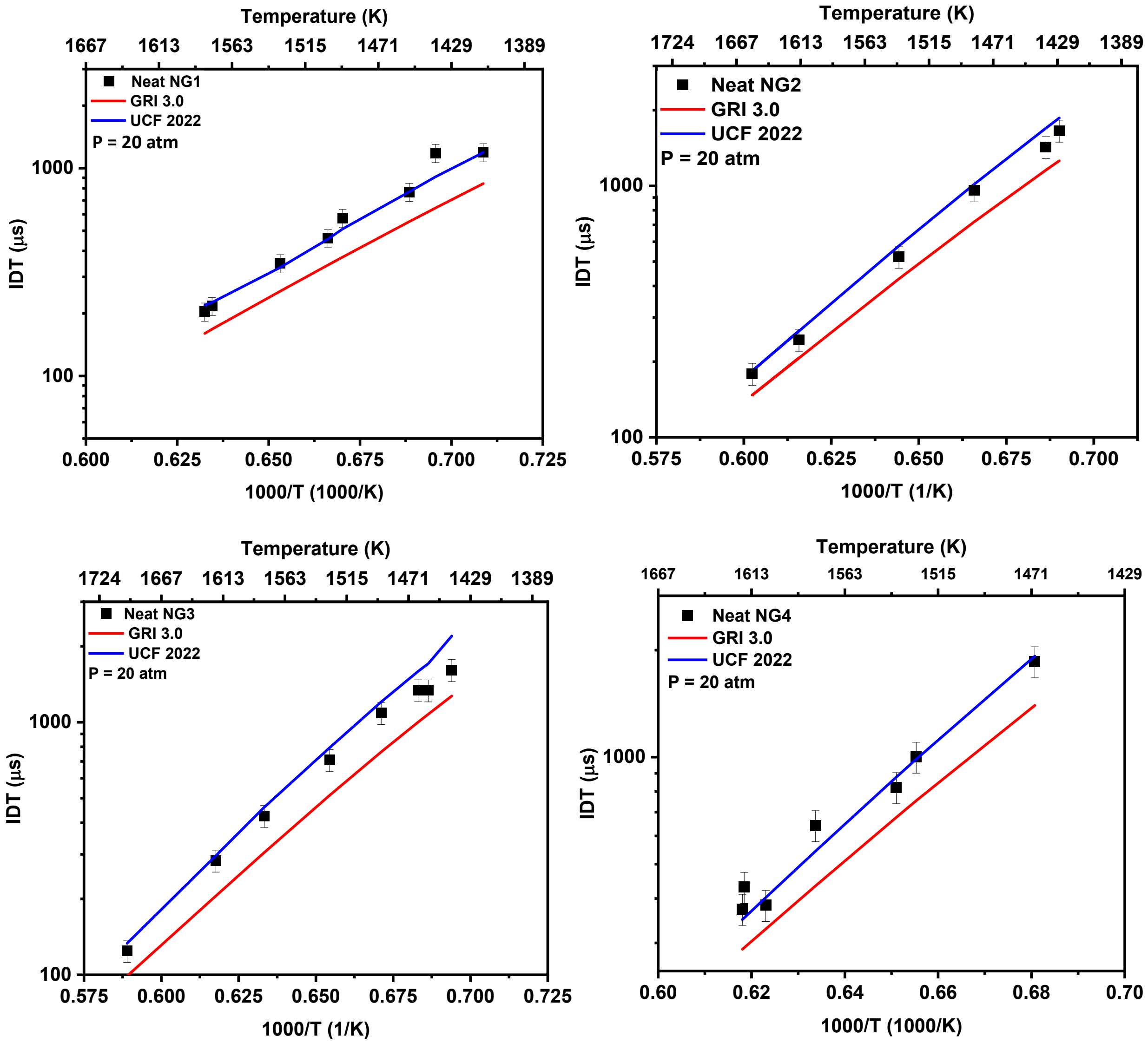

Figure 11: Comparison of experimental IDTs and models during oxidation of NG1 (Top Left); NG2 (Top Right); NG3 (Bottom Left); NG4 (Bottom Right)

Natural Gas + N_2O Mixtures

It can be seen in Figure 12 that with increasing methane purity, the appearance of an impurity such as N_2O has a larger effect on the ignition delay time of the mixture. For example, NG1, which is made up of 93% CH_4 by percent volume, is not largely affected by the addition of N_2O with IDTs remaining within the margin of error throughout the temperature range. However, NG4, which is 98.7% CH_4, more strongly feels the effect of the N_2O impurity. NG4+N_2O sees IDTs decreasing throughout the temperature range just outside of the margin of error, indicating the importance of the nitrogen-carrying reactions on the higher purity natural gas mixtures.

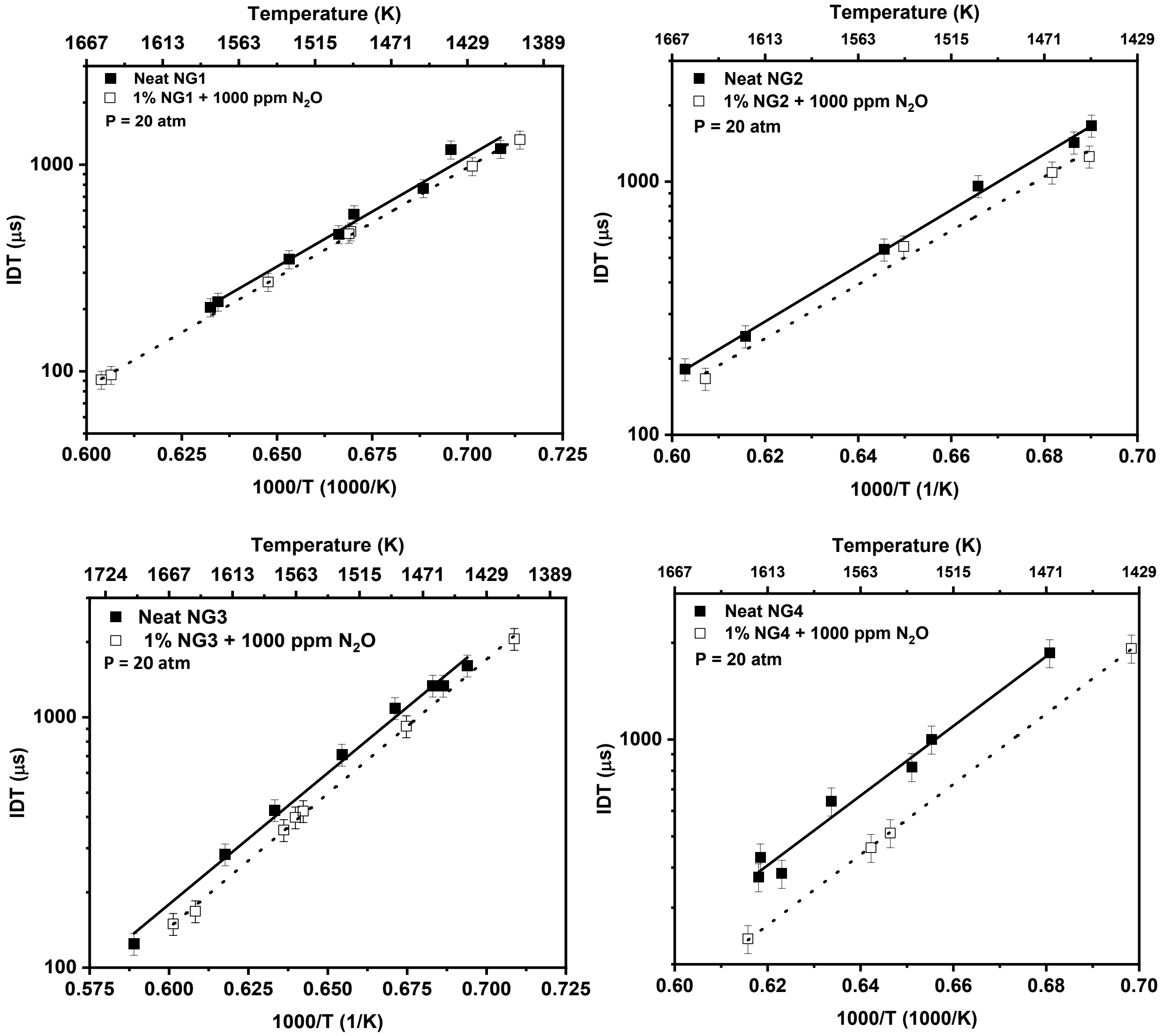

Figure 12: Best Fit Lines of NG1 and NG1+1000 ppm N_2O (Top Left); NG2 and NG2+1000 ppm N_2O (Top Right); NG3 and NG3+1000 ppm N_2O (Bottom Left); NG4 and NG4+1000 ppm N_2O (Bottom Right)

Similar to the neat cases, the NG blends with N_2O addition at 20 atm are also compared to the GRI 3.0 and UCF 2022 mechanisms, results of which can be seen in Figure 13. The same trend can be seen here, where, for each mixture, the UCF mechanism is able to capture the experimental behavior throughout the entirety of the temperature range within the margin of error. The GRI 3.0 mechanism is also largely able to capture the results, with some slight variations in the neat mixtures at lower temperatures, once again indicating the wider variation of mechanism to experimental data at lower temperatures and the importance of temperature on the GRI 3.0 mechanism's behavior.

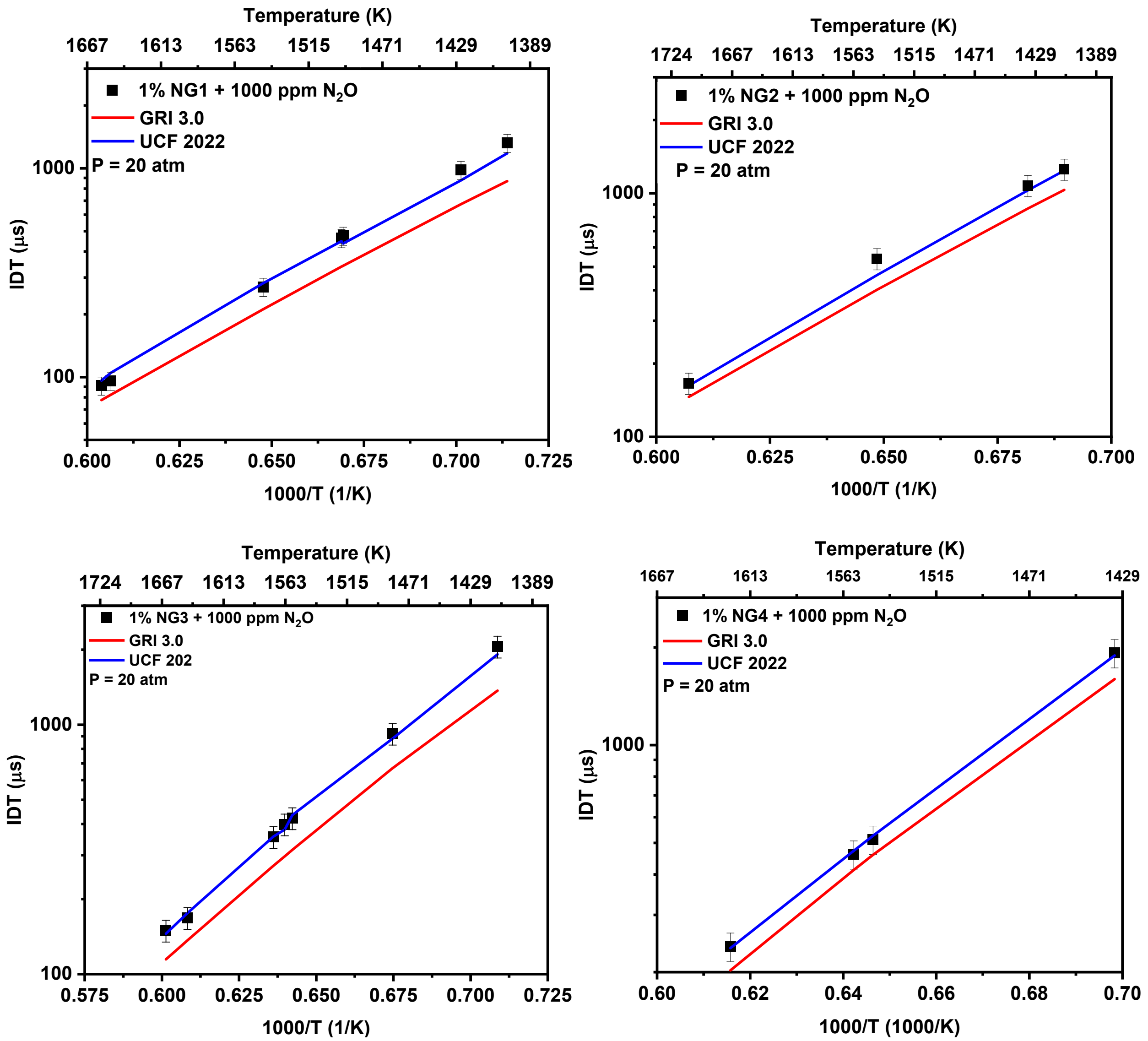

Figure 13: Comparison of experimental IDTs/models during oxidation of NG1+1000 ppm N_2O (Top Left); NG2+1000 ppm N_2O (Top Right); NG3+1000 ppm N_2O (Bottom Left); NG4+1000 ppm N_2O (Bottom Right)

Fuel Rich/Fuel Lean Equivalence Ratios

IDT measurements with an equivalence ratio of 0.5 and 2 were also carried out to represent fuel rich and fuel lean conditions for solely the NG1 blend at 20 atm. The experimental data with best fit lines can be seen in Figure 14. It was found that a lower equivalence ratio resulted in quicker ignition delay times while a high equivalence ratio resulted in slower ignition.

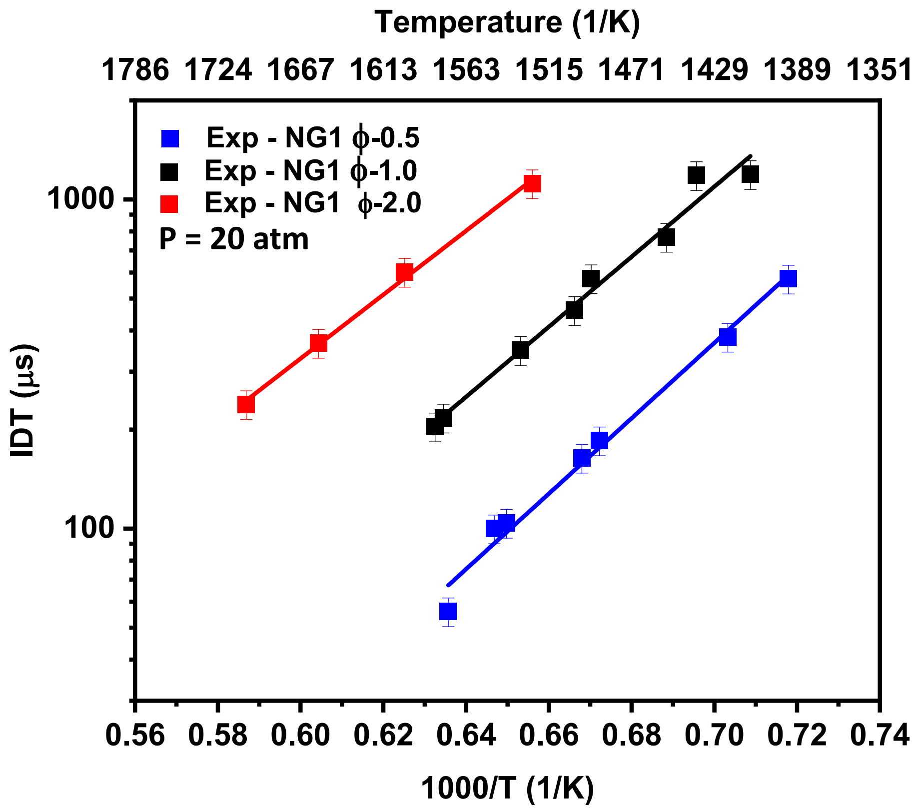

Figure 14: Comparison of shock tube IDTs at varying equivalence ratios during NG oxidation at 20 atm with best fit lines

A comparison of the three equivalence ratios at 20 atm with their complementary GRI 3.0 and UCF 2022 chemical kinetic mechanism simulations can be seen Figure 15. It was found that, overall, the GRI mechanism underpredicts the IDT for all three equivalence ratios while the UCF mechanism is largely able to capture the experimental behavior throughout the range of equivalence ratios and temperatures, with slight variation appearing at the Φ=0.5 low temperature condition, once again indicating the dependence of the mechanism on temperature.

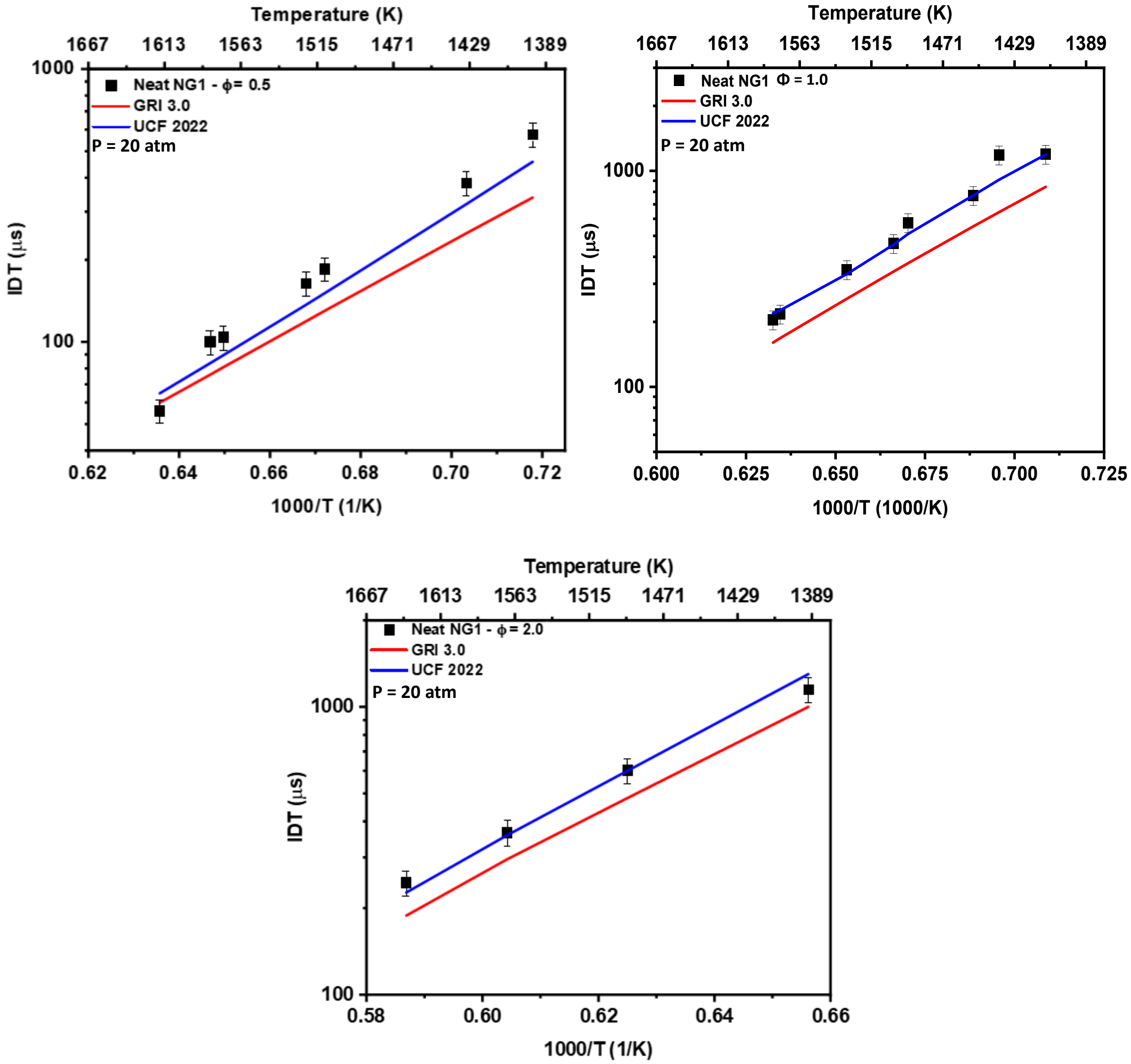

Figure 15: Comparison of shock tube IDTs during oxidation of NG1 at Φ=0.5 (Top Left); Φ=1 (Top Right); Φ=2.0 (Bottom)

Carbon Monoxide Time Histories

Neat Natural Gas Mixtures

Figure 16 shows a comparison between CO production during combustion of natural gas mixtures at low and high temperature conditions. In general, each mixture shows the expected trend of the elevated temperature condition resulting in faster CO formation. The elevated temperature and pressure due to the combustion process causes natural gas to oxidize rapidly, leading to the steep increase in CO mole fraction seen in the high temperature conditions.

Comparing between NG blends is more difficult since each temperature condition was individually selected based on the available data points (i.e., the high temperature condition for NG1 is much lower than that of the other NG blends), making it more difficult to draw a direct comparison. Generally, at similar temperature conditions, the higher the CH_4 concentration, the longer it takes CO to form and less CO will form. This trend can best be seen in an upcoming section.

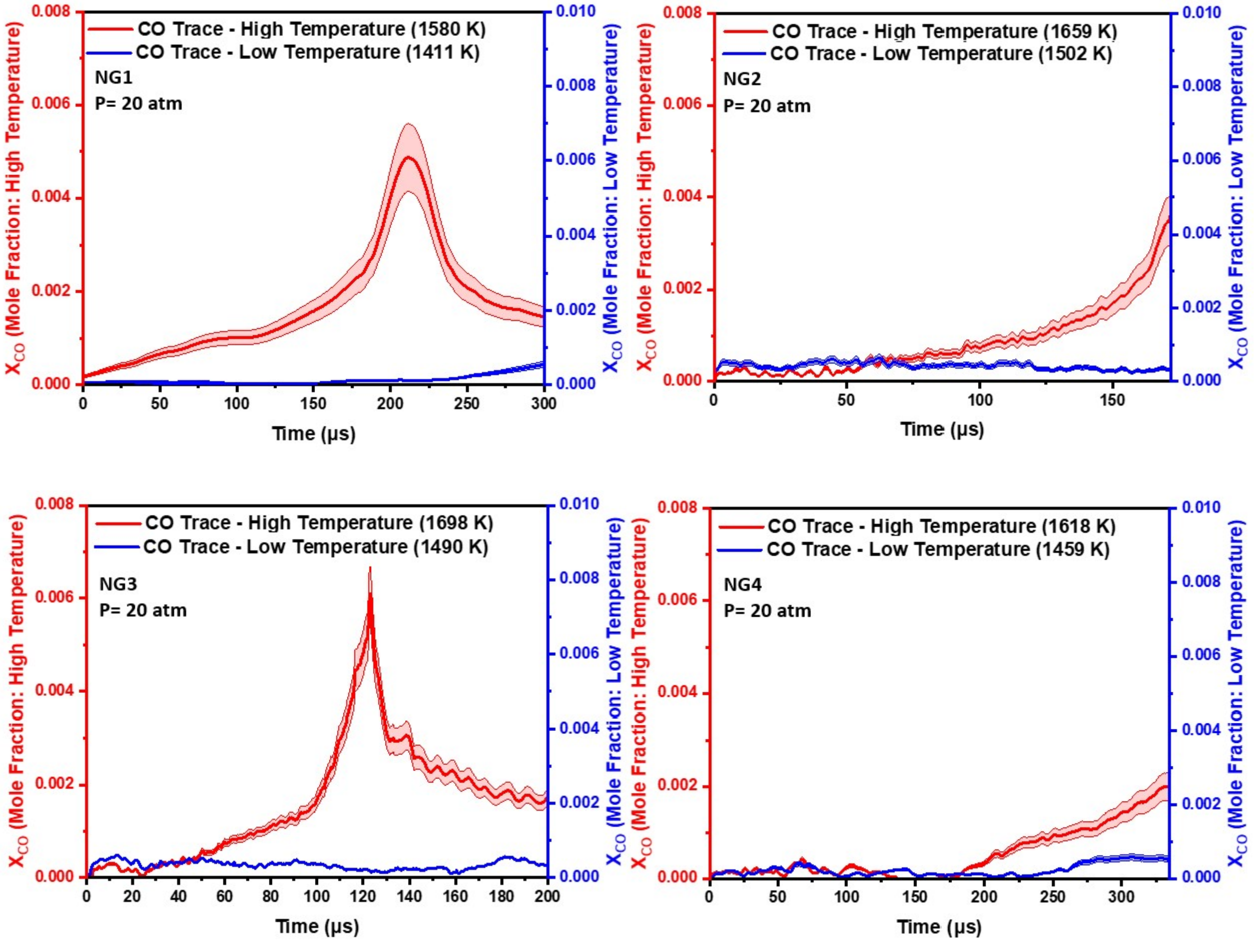

Figure 16: CO formation at low and high temperature for NG1 (Top Left); NG2 (Top Right); NG3 (Bottom Left); NG4 (Bottom Right)

The experimental data obtained for CO time histories was also used to validate the UCF 2022 model. The results are shown in Figure 17 with the UCF 2022 model in dashes and the GRI 3.0 model in dots. For most cases, specifically NG2, NG3, and NG4, the UCF model is largely able to capture the initial formation of CO with variations beginning to show towards the peak as the mechanism predicts slightly higher/faster CO formation. The GRI 3.0 mechanism does capture some of the early CO formation, but deviates more drastically than the UCF 2022 mechanism once the formation rate increases, predicting both a higher CO mole fraction and quicker formation.

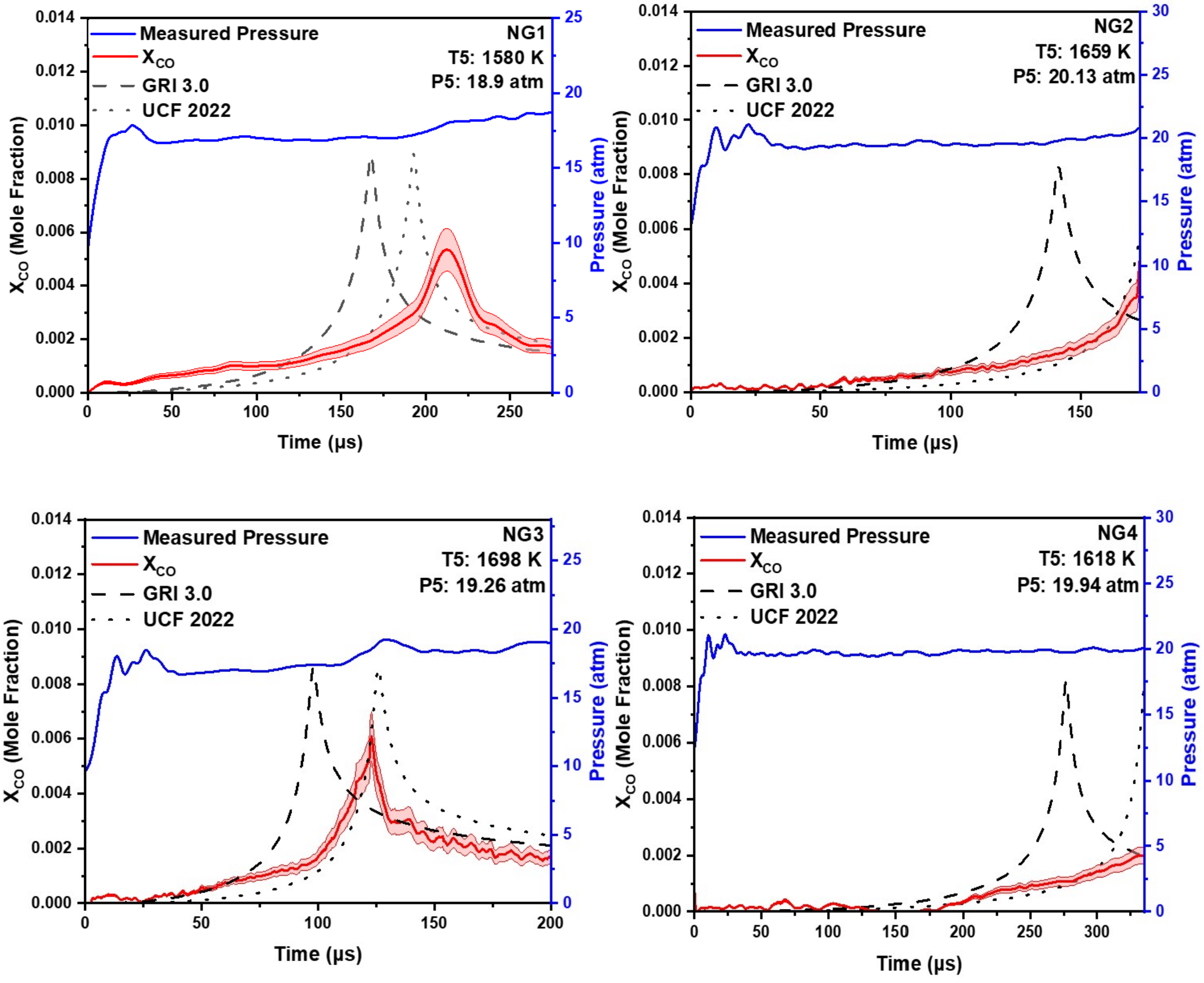

Figure 17: Comparison of CO Time Histories Predicted by GRI 3.0 and UCF 2022 Models with Experimental Results of NG1 (Top Left); NG2 (Top Right); NG3 (Bottom Left); NG4 (Bottom Right)

Natural Gas + N_2O Mixtures

When comparing N_2O addition to the neat cases, it is found that at the low temperature conditions, there is little difference in CO production when compared to the baseline mixtures. This is likely due to the low amount of N_2O added (1000 ppm) and could indicate that these reactions are not as sensitive at lower temperatures. For the high temperature conditions, the addition of N_2O to both NG2 and NG4 results in the formation of CO occurring both more quickly and in higher amounts through the end of the test time. This once again indicates the dependence of the mechanism on temperature. These trends can be seen in Figure 18.

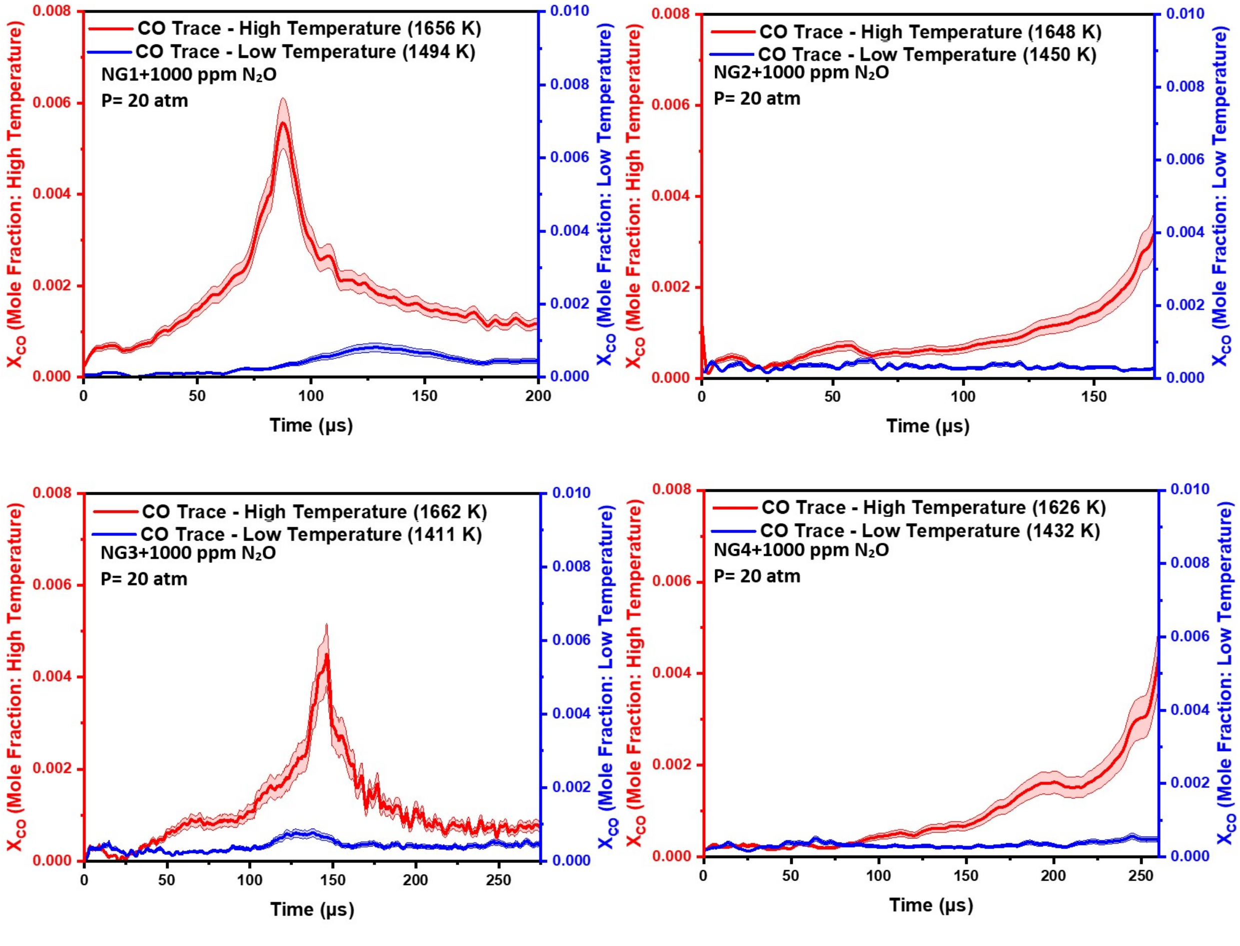

Figure 18: CO formation at low and high temperature for NG1+N_2O (Top Left); NG2+N_2O (Top Right); NG3+N_2O (Bottom Left); NG4+N_2O (Bottom Right)

Again, these N_2O addition cases were also compared against the UCF 2022 and GRI 3.0 mechanisms and the results can be seen in Figure 19. The N_2O addition mixtures follow a similar trend to the neat case where both models are able to capture early behavior and then begin to show variations later in the test time, predicting faster CO formation and overpredicting CO peak values. These cases are also similar to the neat NG mixtures as the GRI 3.0 mechanism does again deviate more drastically than the UCF 2022 mechanism once the formation rate increases, predicting higher CO mole fraction formation and faster reactions.

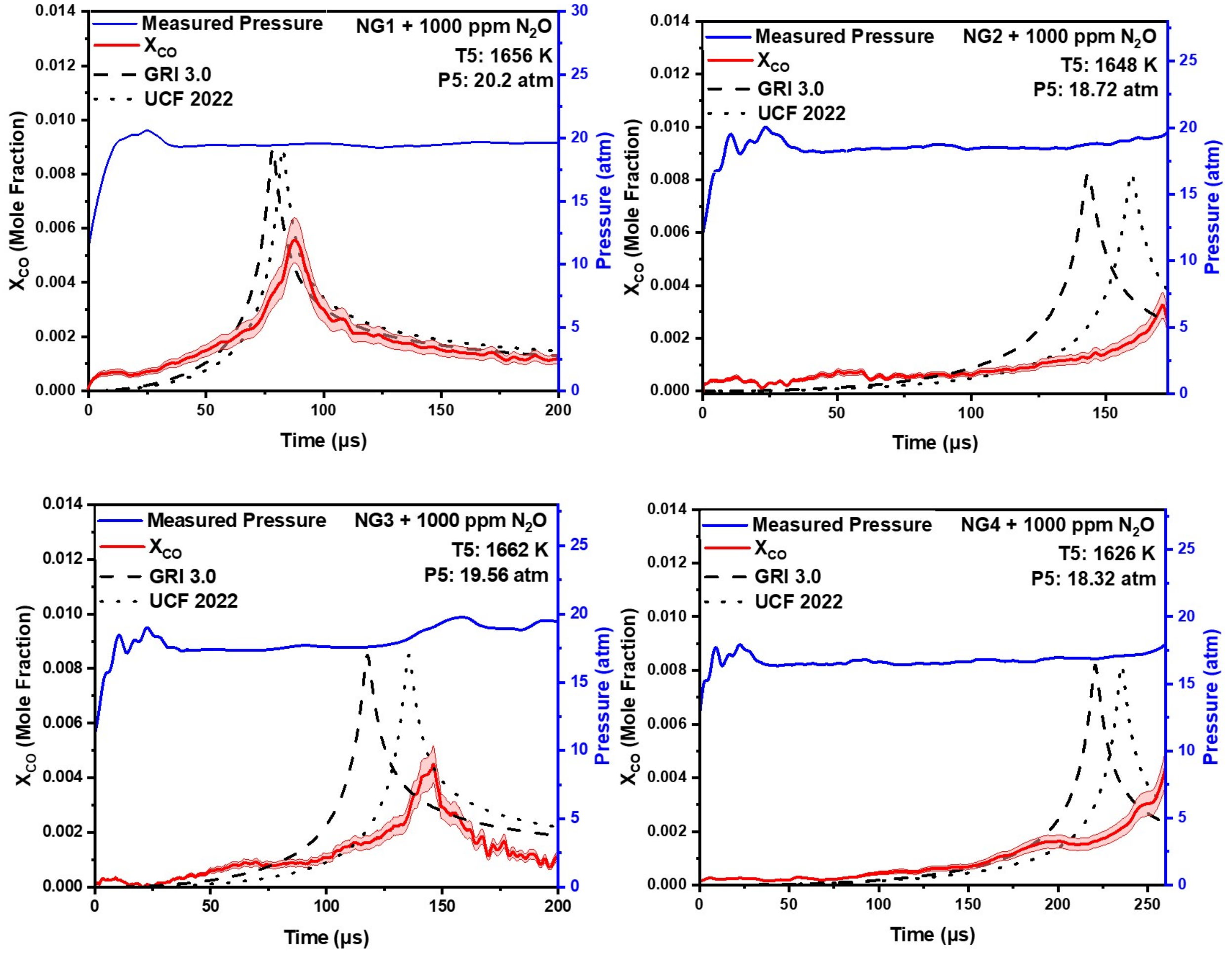

Figure 19: Comparison of CO Time Histories Predicted by GRI 3.0 and UCF 2022 Models with Experimental Results of NG1+1000 ppm N_2O (Top Left); NG2+1000 ppm N_2O (Top Right); NG3+1000 ppm N_2O (Bottom Left); NG4+1000 ppm N_2O (Bottom Right)

Sensitivity Analysis

The mechanism selected for use during the sensitivity analysis is the UCF 2022 mechanism. This was selected because, while both mechanisms match at certain conditions, the UCF mechanism is closer to the experimental data more often. OH* sensitivity analyses were carried out in order to identify key reactions that affect the ignition delay times of methane/natural gas mixtures. IDT sensitivity analyses were conducted at the time corresponding to when half of the fuel (CH_4) had decomposed. This process was carried out focusing on the critical reactions and the specific reactions of interest were isolated. A positive sensitivity indicates increased ignition delay times (lower reactivity) while a negative sensitivity value indicates lower ignition delay times and higher reactivity. The trends seen in the sensitivity studies remain true for all NG mixtures and, as such, only NG2 will be shown for brevity.

First comparing the NG2 mixtures for the low and high temperature cases, it is apparent that the scales of the reactions are quite different. While the top reactions are very similar, the $2CH_3 => C_2H_6$ reaction goes from a sensitivity coefficient of 27.4 at 1400 K to a sensitivity coefficient of 0.7 at 1700 K showing a large dependence on temperature. With the addition of N_2O as an impurity, nitrogen-carriers and reactions begin to appear, though the top reactions seen in the neat cases still carry over. The bottom two graphs highlight the nitrogen reactions and a similar trend from the neat NG2 mixtures can be seen when comparing between low and high temperatures. The $N_2O(+M)=N_2+O(+M)$ reaction has a sensitivity coefficient of -9.2 at 1400 K to -0.28 at 1700 K. Results can be seen in Figure 20 for the neat case, and Figure 21 for the NG2+N_2O addition.

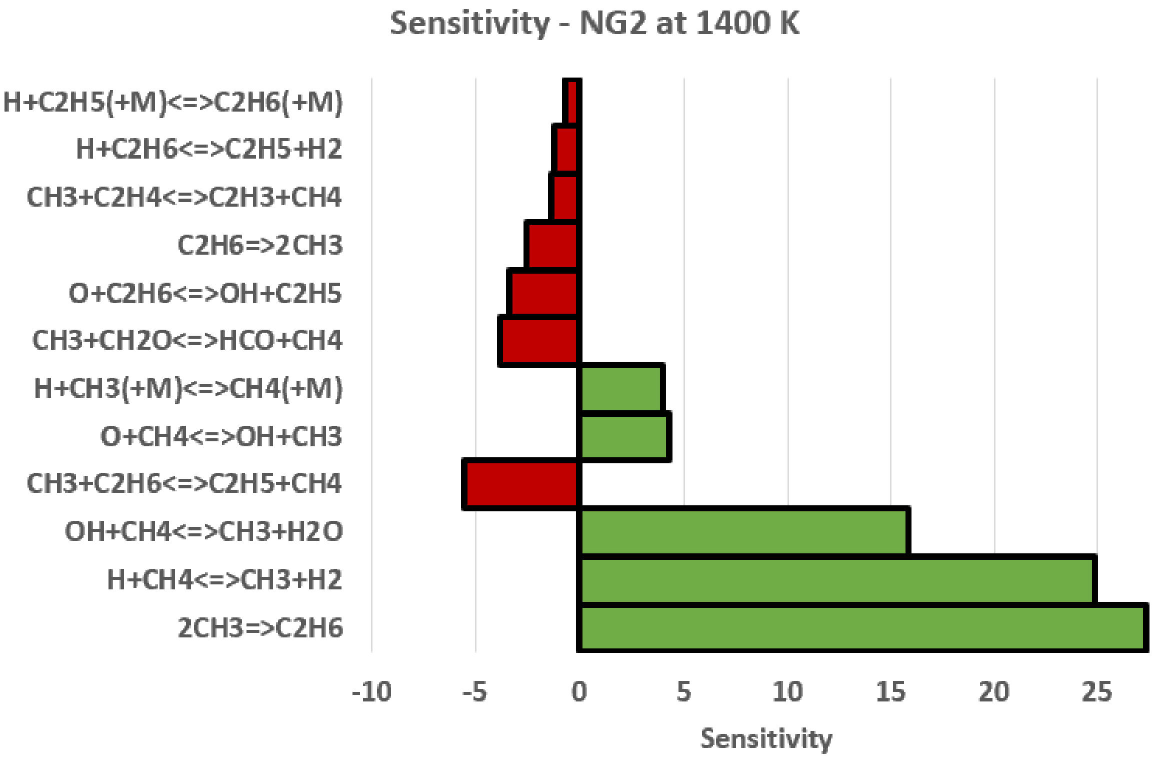

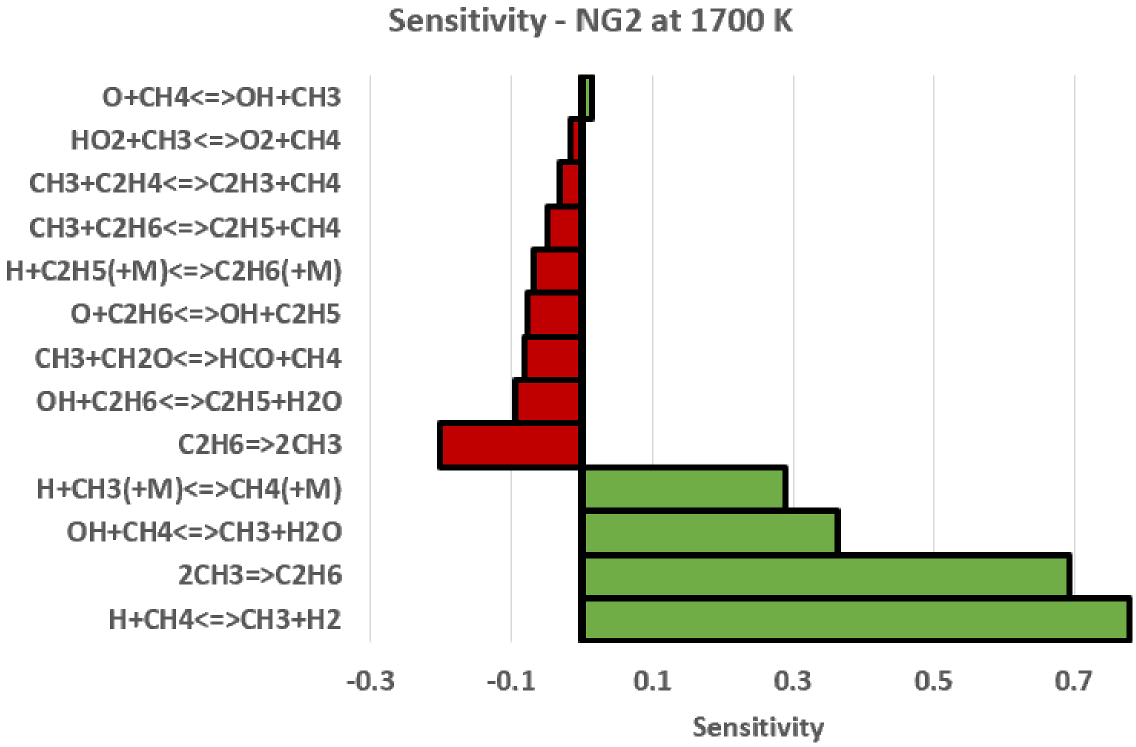

Figure 20: IDT Sensitivity analysis for NG2 for 20 atm at 1400 K (Top); at 1700 K (Bottom)

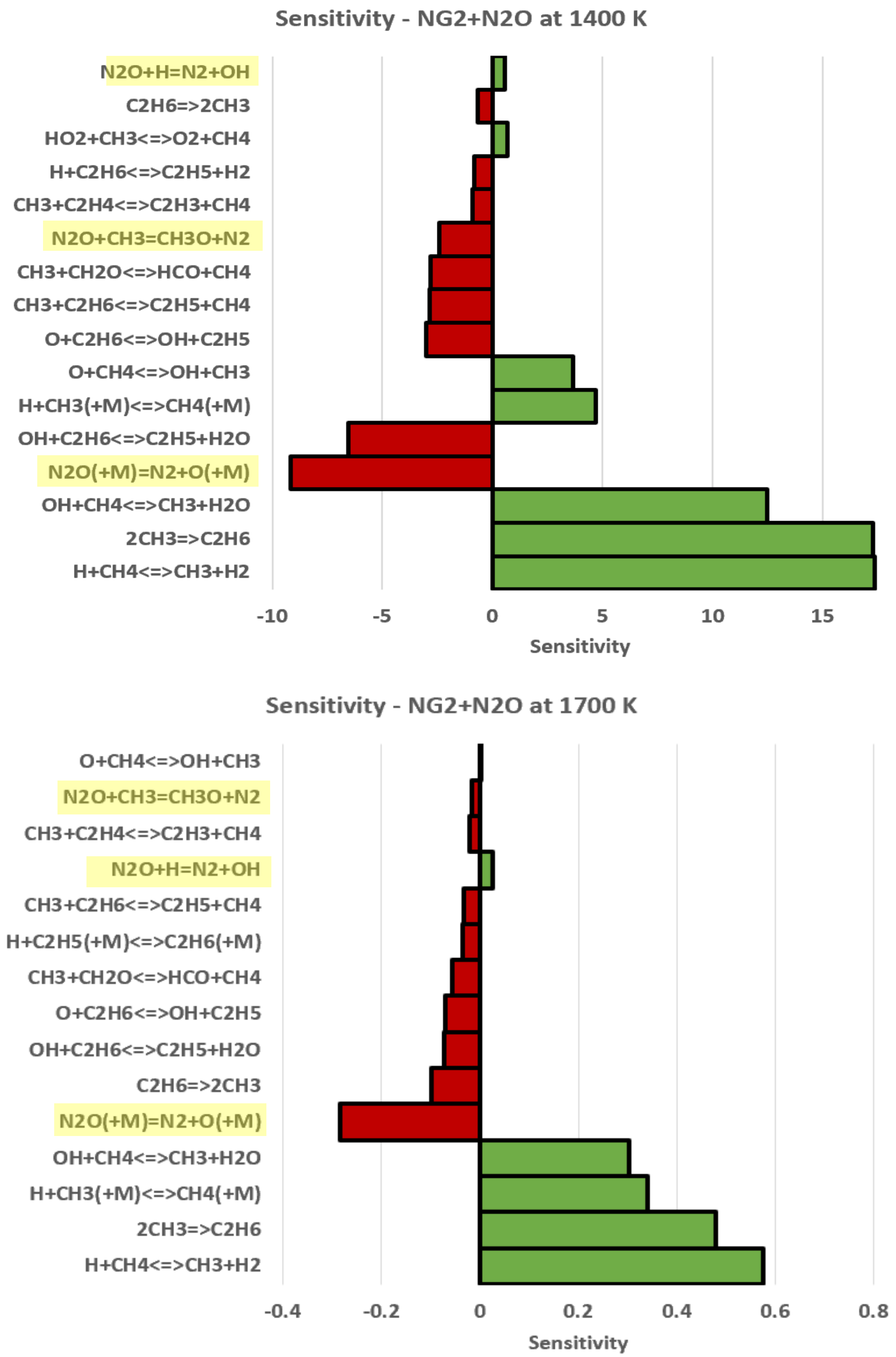

Figure 21: IDT Sensitivity analysis at 20 atm for NG2+1000 ppm N_2O at 1400 K (Top); at 1700 K (Bottom)

Reaction Pathway Analysis

The reaction path analysis was carried out for mixture 2 for oxidation of natural gas in order to understand important reaction pathways involved in CO formation and fuel decomposition. Since natural gas consists of multiple fuels, a reaction pathway analysis was carried out selecting CH_4, C_2H_6, and C_3H_8 each individually as the starting fuel and ending with CO in order to compare the effects of higher hydrocarbons on the reaction pathways. Similar trends are seen throughout the pressure range, so the 20 atm experiments will be the only section showing all 3 starting fuels individually. The UCF 2022 reaction mechanism was used for reaction path analysis as it predicted IDTs with a good degree of accuracy.

CH_4 Decomposition

Methane was first selected for use as the primary fuel and its decomposition pathways will be discussed in the following sections. A high and low temperature pathway analysis was carried out to investigate the effects of temperature on the decomposition pathways, but the pathways between the temperature conditions was found to be extremely similar. Trends were comparable since, as seen in the sensitivity analysis, the reactions have large overlap, with the sensitivity coefficient being the main change between temperatures. As such, the 1400 K condition will be the focus. Again, similar trends are seen throughout the various starting fuels, and, as such, this will hold true for C_2H_6 and C_3H_8 investigations.

The initiation of methane combustion in a natural gas oxidation mixture at 1400 K begins with the unimolecular decomposition of methane at low temperatures resulting in the formation of CH_3. This process at the low temperature condition readily forms H, O, and OH radicals in the presence of oxygen. The high concentration of these radicals in the natural gas oxidation mixture speeds up the decomposition of methane by hydrogen abstraction and reactions R1-R3. The methyl radical (CH_3) proceeds to react with the free O-atom radicals to form CH_2O via reaction R4, as well as an additional reaction pathway that sees CH_3 react with a third body to release CH_2 (reaction R5). In the first branch, CH_2O forms HCO via hydrogen abstraction and third body interactions (R6, R7) and then either terminates in CO formation via reactions R8 and R9 (a third body reaction and additional H-atom abstraction), or forms CO_2 by interacting with the free O radicals (R10). In the second branch, CH_2 either oxidizes to form CO_2, or reacts with the free O radicals to form HCO, then terminating in CO formation as discussed above (R11, R12). Finally, CO_2 reacts with H-atom radicals and additional third-bodies to decompose into CO via reactions R13 and R14. The reactions are listed in Table 4 and the reaction/decomposition pathways can be seen in Figure 22.

Table 4: Reactions for 1400 K, 20 atm, CH_4 decomposition of NG2

R1	H+CH4 = CH3+H2	**R8**	HCO(+M) = CO+H(+M)
R2	O+CH4 = OH+CH3	**R9**	HCO+H = CO+H2
R3	OH+CH4 = CH3+H2O	**R10**	HCO+O = CO2+H
R4	CH3+O = CH2O+H	**R11**	CH2+O2 = CO2+2H
R5	CH3(+M) = CH2+H(+M)	**R12**	CH2+O = HCO+H
R6	CH2O+H = HCO+H2	**R13**	CO2+H = CO+OH
R7	CH2O(+M) = HCO-H(+M)	**R14**	CO2(+M) = CO+O(+M)

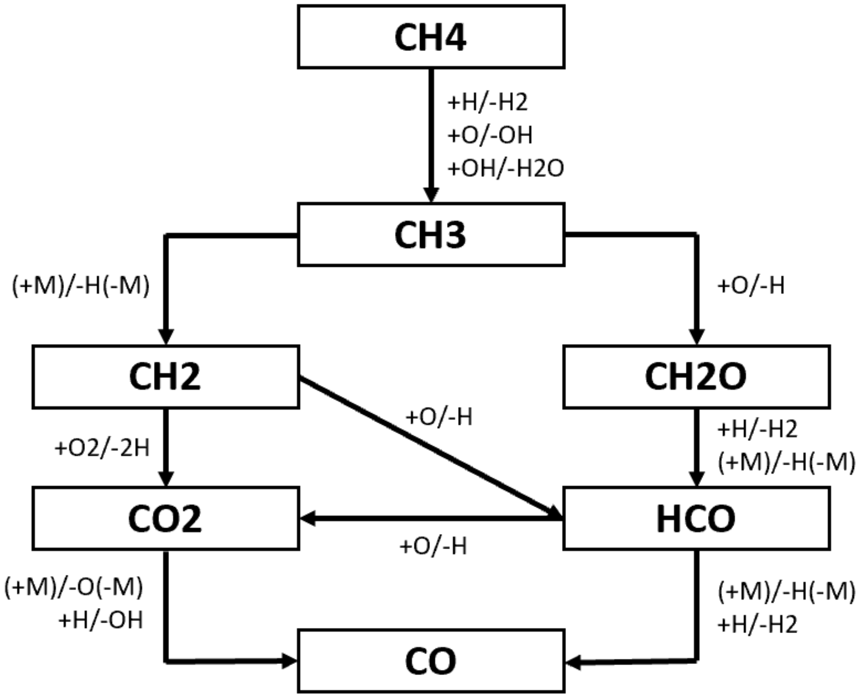

Figure 22: Major reaction pathways to CO for 1400 K, 20 atm, CH_4 decomposition of NG2

An additional reaction pathway analysis was carried out for the NG2+1000 ppm N_2O case. For N_2O addition, trends were once again comparable since, as seen in the sensitivity analysis, the reactions have large overlap, with the sensitivity coefficient being the main change between temperatures. As such, the N_2O addition reaction pathway analysis will be only at the 1400 temperature condition and only for NG2. Figure 23 shows the reaction pathway diagram for this case, with the pathway in blue taking place only with N_2O addition.

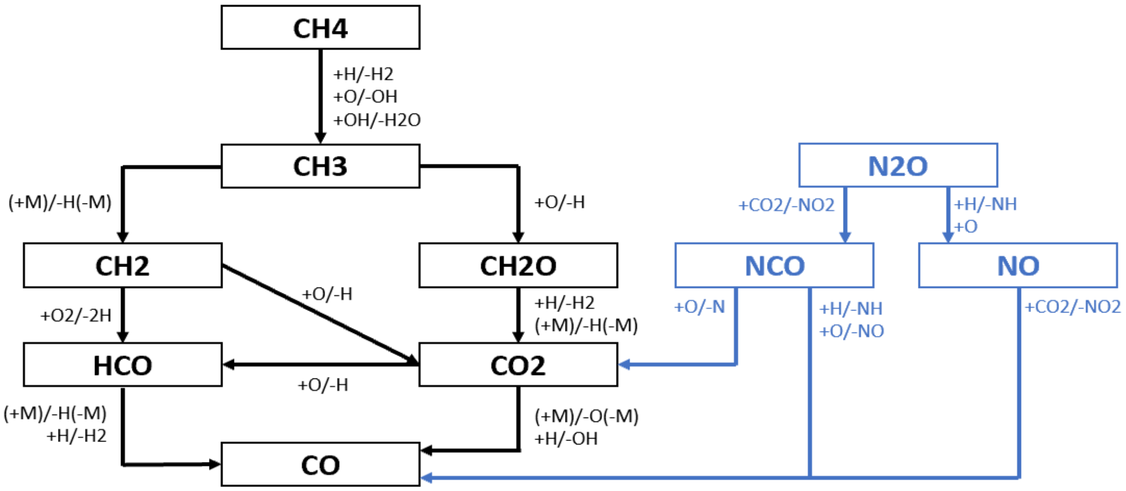

Figure 23: Major reaction pathways to CO for 1400 K, 20 atm, CH_4 decomposition of NG2+1000 ppm N_2O

The methane reaction pathway for natural gas oxidation with N_2O addition is similar. The reactions R1-R14 remain constant and are the primary method for CO formation. As for the N_2O-specific reactions, N_2O first decomposes into with NCO via reacting with CO_2 or NO by reacting with either a hydrogen-atom or oxygen-atom radical (RN1-RN3). NO then reacts with CO_2 to terminate in the formation of the CO molecule (RN4). NCO has two possible branches. The molecule can release a nitrogen radical and form CO_2 (then following the R13 and R14 reaction path to CO) or directly form CO by reacting with either a hydrogen-atom or oxygen-atom radical (RN5-RN7). The N_2O-specific reactions are listed in Table 5.

Table 5: Reactions for 1400 K, 20 atm, CH_4 decomposition of NG2+1000 ppm N_2O

RN1	N2O+CO2 = NO2+NCO
RN2	N2O+H = NO + NH
RN3	N2O+O = 2NO
RN4	CH2NO+CO2 = NO2+CO
RN5	NCO+O = CO2+N
RN7	NCO+H = CO+NH
RN8	NCO+O = CO+NO

C_2H_6 Decomposition

Utilizing ethane as the starting fuel, there are now additional interactions as a result of the higher hydrocarbons. Ethane decomposition in the NG2 oxidation mixture at 1400 K begins with the interaction of ethane with H, O, and OH radicals resulting in the formation of C_2H_5 via reactions R15-R17. C_2H_5 proceeds to branch into three different paths. The first path features C_2H_5 reacting with the free O-atom radicals to release CH_3 and form CH_2O via reaction R18. From here, CH_2O decomposition into the final product of CO by following the process described above, reactions R6-R9. In the second path, C_2H_5 undergoes a third-body reaction to release a H atom and form C_2H_4 (R19).C_2H_4 then releases additional CH_3 radicals via interactions with O-atom radicals, resulting in HCO formation (R20). HCO then disassociates and forms CO in the same reaction pathway described in the CH_4 decomposition section above (R8, R9). The final branch sees C_2H_5 interacting with the H-atom radical and releasing two CH_3 radicals via reaction R21. From CH_3, the same reactions are undergone, resulting in the formation of CO as described above and in reactions R4-R14. The additional new reactions are listed in Table 6 and the pathways can be seen in Figure 24.

Table 6: Reactions for 1400 K, 20 atm, C_2H_6 decomposition of NG2

R15	H+C2H6 = C2H5+H2	**R19**	C2H5(+M) = C2H4+H(+M)
R16	O+C2H6 = OH+C2H5	**R20**	C2H4+O = HCO+CH3
R17	OH+C2H6 = C2H5+H2O	**R21**	C2H5+H = 2CH3
R18	CH2O+O = CH2O+CH3		

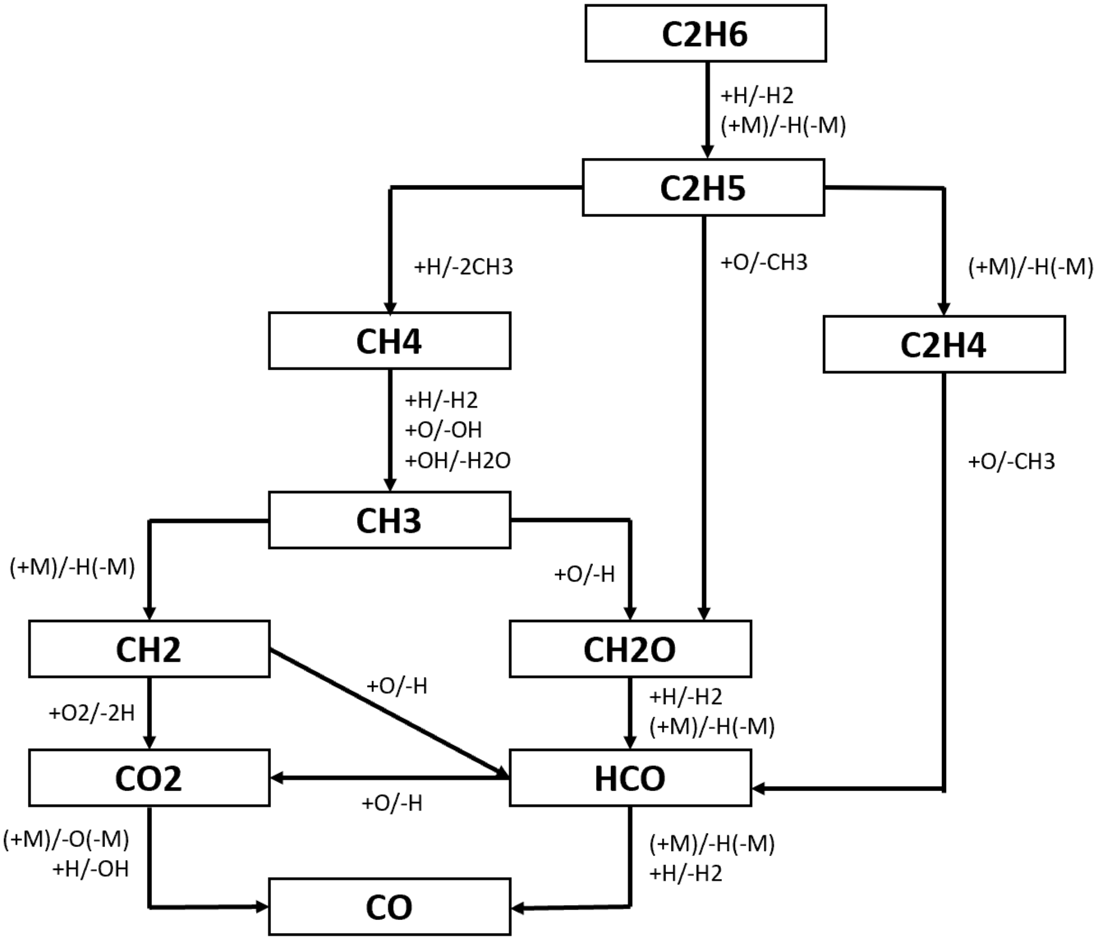

Figure 24: Major reaction pathways to CO for 1400 K, 20 atm, C_2H_6 decomposition of NG2

C_3H_8 Decomposition

Finally, selecting C_3H_8 as the starting fuel results in even more interactions as a result of the increased carbon and hydrogen atoms. Decomposition of C_3H_8 in NG2 at 1400 K begins with the formation of C_2H_5 and C_3H_7; hydrogen abstraction releases C_3H_7 and third body interactions with C_3H_8 forms C_2H_5 as well as the methyl radical (R22, R23). These larger hydrocarbons will then react further, releasing additional radicals, including multiple methyl radicals. For example, C_3H_7 will react with the H-atom radical, forming both the methyl radical and C_2H_5 in reaction R24. C_3H_7 will also experience a third body reaction, resulting in the formation of CH_3 once again (reaction R25). On the other hand, C_2H_5 will interact with an oxygen-atom radical, resulting in the formation of a methyl group as well as CH_2O; an additional path for

C_2H_5 includes the interaction of the molecule with a hydrogen-atom radical, which results in the formation of two methyl radical groups (R26, R27).

From CH_3, the same reaction pathway from the CH_4 and C_2H_6 starting fuels also exists (reactions R4-R14), but due to the increase in methyl groups, there are additional, more prevalent reaction pathways which will be addressed. The methyl group will react to form CH_2OH and then CH_2O (R28, R29). CH_2O can then form HCO from hydrogen abstraction or third-body interactions, or directly form CO (R30-R32). Finally, HCO will experience additional hydrogen abstraction and third body interactions to terminate the reaction with the formation of CO (R33, R34). The additional new reactions are listed in Table 7 and the pathways can be seen in Figure 25.

Table 7: Reactions for 1400 K, 20 atm, C_3H_8 decomposition of NG2

R22	C3H8+H= C3H7+H2	**R29**	CH2OH(+M) = CH2O+H(+M)
R23	C3H8(+M) = C2H5+CH3(+M)	**R30**	CH2O+H = HCO+H2
R24	C3H7+H = CH3+C2H5	**R31**	CH2O(+M) = HCO+H(+M)
R25	C3H7(+M) = C2H4(+M)	**R32**	CH2O(+M) = CO+H2(+M)
R26	C2H5+H = 2CH3	**R33**	HCO(+M) = CO+H(+M)
R27	C2H5O+O = CH2O+CH3	**R34**	HCO+H = CO+H2
R28	CH3+OH = CH2OH+H		

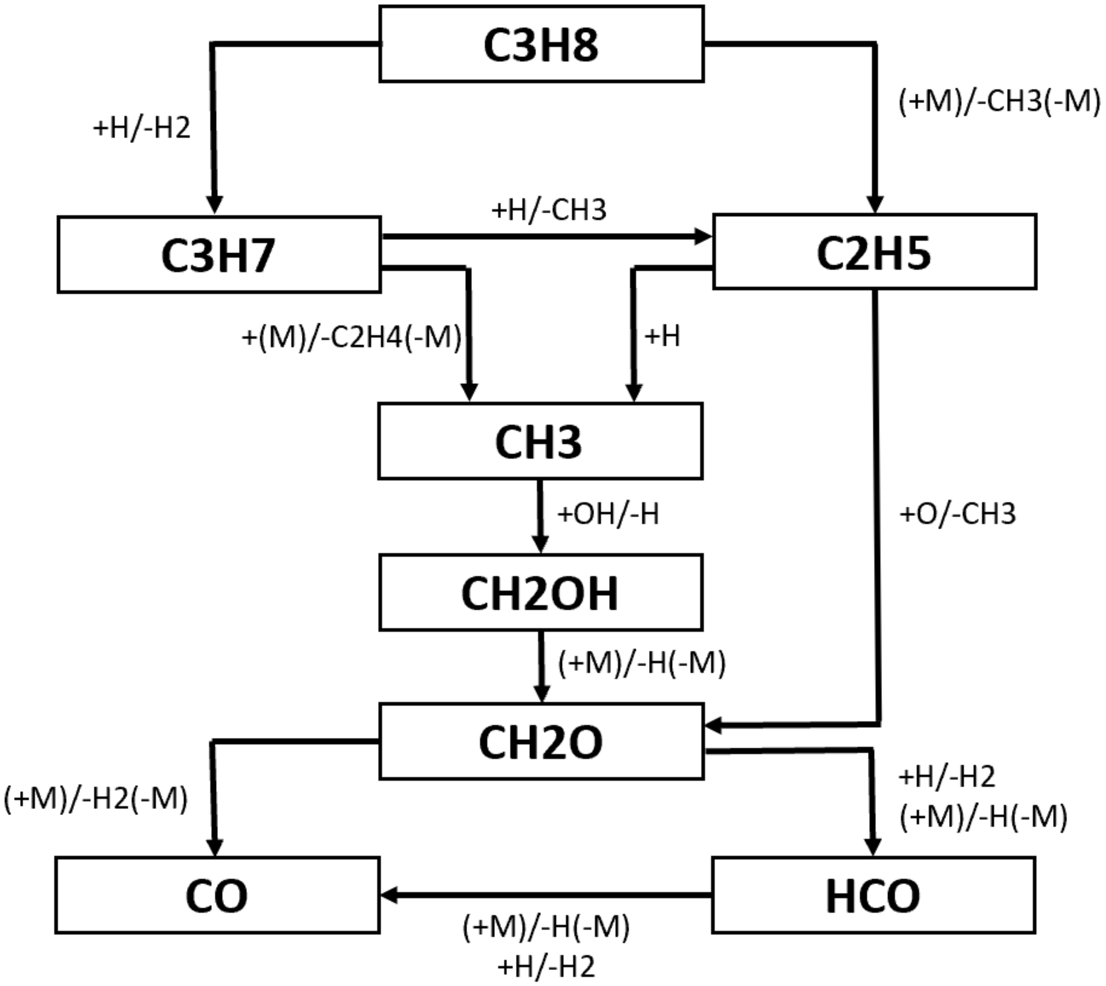

Figure 25: Major reaction pathways to CO for 1400 K, 20 atm, C_3H_8 decomposition of NG2

Intermediate Pressure Natural Gas Blends

Ignition Delay Times

Shock tube ignition delay times of various blends of natural gas at 50 atm are offered as a comparison to observe the effect of methane purity on LNG fuels. The experimental data with best fit lines can be seen in Figure 26. As a baseline check, the obvious trend of elevated temperature resulting in quicker IDT for every mixture is confirmed. It was also found that, when comparing various blends of natural gas, higher CH_4 purity levels generally result in an increase in ignition delay time. In comparison to the 20 atm experiments, the margin of error is much smaller with NG2, NG3, and NG4 largely overlapping throughout the temperature range with only the 93% methane-purity NG1 blend being outside of the margin of error. This indicates that at higher pressures, the effect of methane purity in the natural gas blends may not be as prominent, at least for higher purity mixtures.

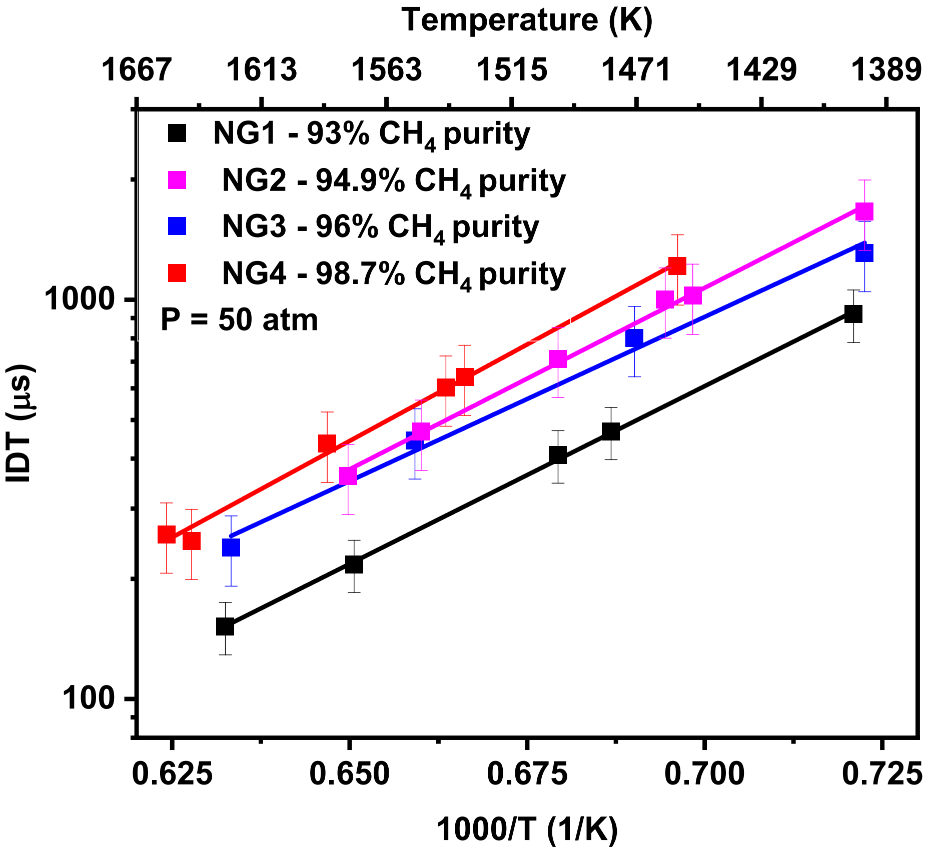

Figure 26: Comparison of shock tube IDTs during NG oxidation at 50 atm with best fit lines

Figure 27 shows the model comparison for all neat NG mixtures at 50 atm with the UCF 2022 mechanism shown in blue and the GRI 3.0 mechanism in red. While for the 20 atm condition, the mechanism was able to largely capture the entirety of the experimental behavior throughout the temperature range, the 50 atm condition begins to show some variation. It can be seen that the UCF 2022 mechanism matches the experimental points well for the NG1 mixture, but for NG2, NG3, and NG4, the mechanism begins to overpredict the IDTs just barely on the margin of error. The overprediction is also largely standard throughout the temperature range, not varying based on a low or high temperature condition. The GRI 3.0 mechanism underpredicts the IDTs for each case. This indicates the importance of pressure on mechanism performance.

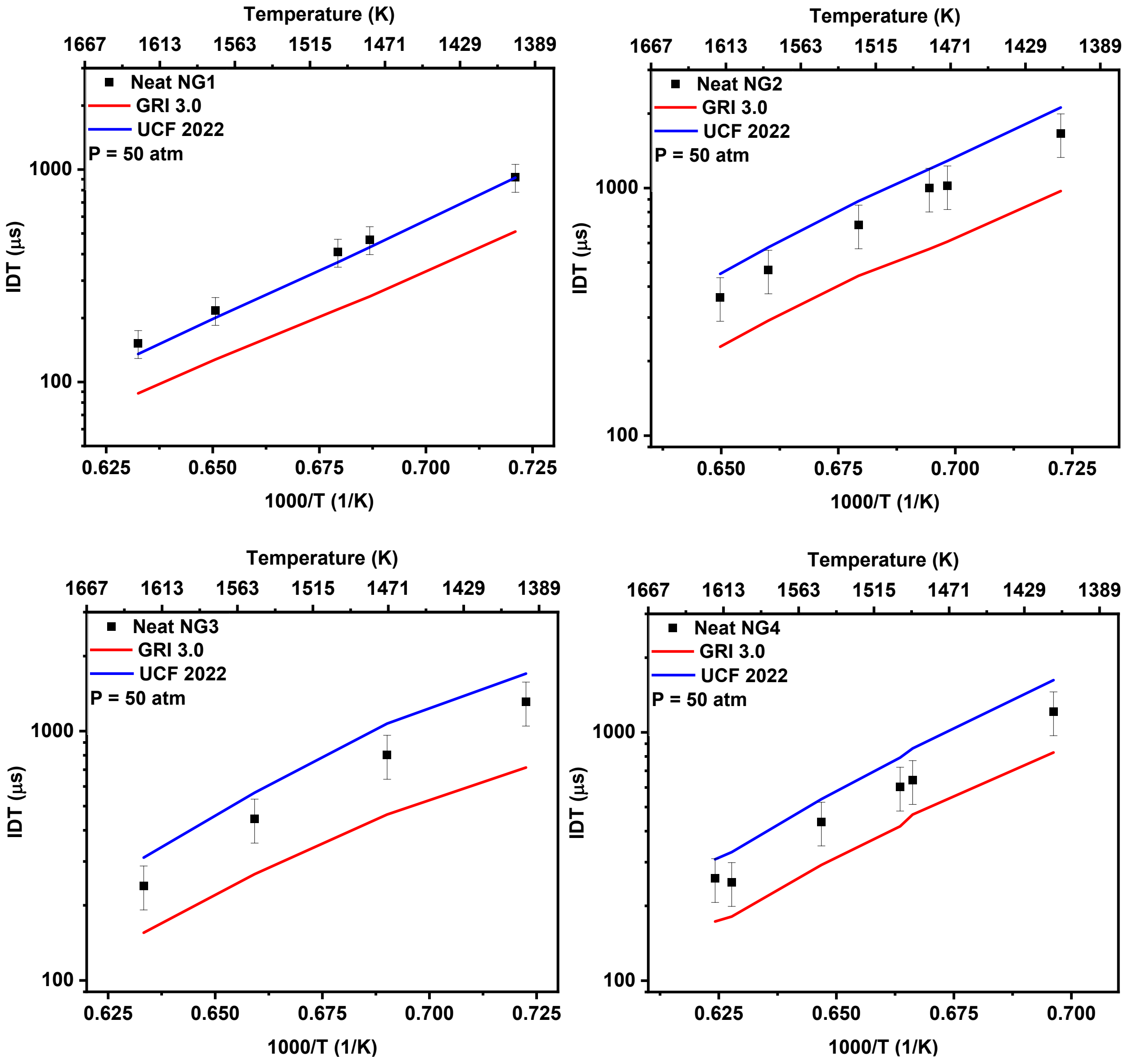

Figure 27: Comparison of 50 atm experimental IDTs and models during oxidation of NG1 (Top Left); NG2 (Top Right); NG3 (Bottom Left); NG4 (Bottom Right)

Sensitivity Analysis

The UCF 2022 mechanism is once again used for the 50 atm sensitivity analysis and the analysis was carried out in the same way as described in the low-pressure sensitivity analysis section. Again, trends in the sensitivity studies hold true for all NG mixtures and, as such, only NG2 will be shown.

Similar to the 20 atm condition, when comparing the NG2 mixtures for the low and high temperature cases, the scales of the reactions are very different. While the top reactions are similar, the $2CH_3{=>}C_2H_6$ reaction goes from a sensitivity coefficient of 32.0 at 1450 K to a sensitivity coefficient of 0.64 at 1700 K showing a large dependence on temperature. Comparing this 50 atm pressure case to the lower, 20 atm analysis, it can be seen that, in general, most of the higher-pressure reactions are less sensitive in comparison to their lower pressure counterparts. This aligns with the results seen in the IDTs, indicating that, at these intermediate pressures, the effect of methane purity in natural gas blends is not as prevalent as it is at lower pressures. The sensitivity results can be seen in Figure 28.

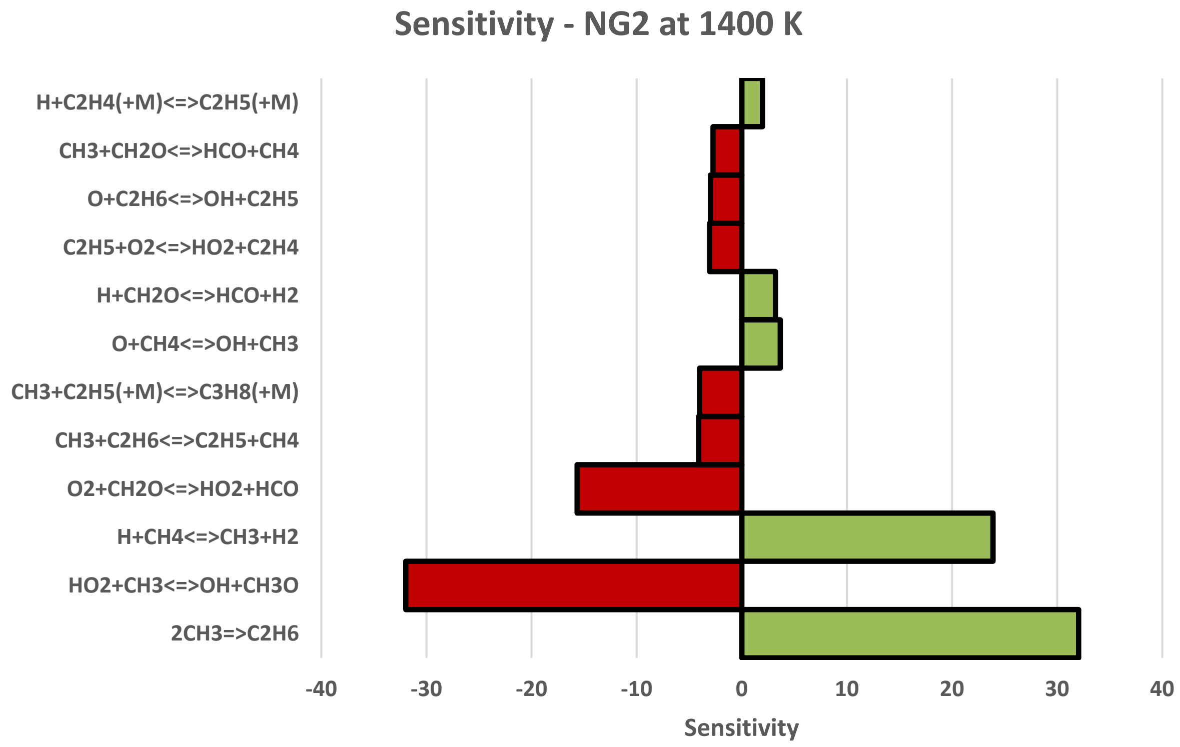

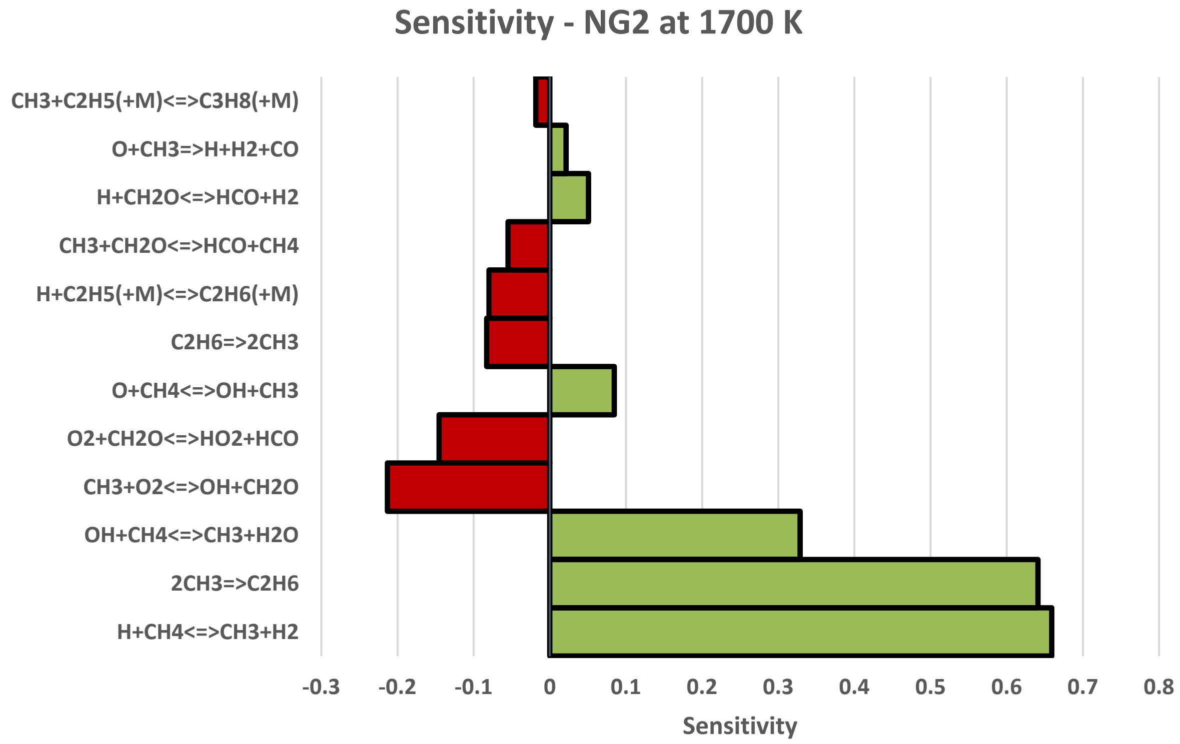

Figure 28: IDT Sensitivity analysis at 50 atm for NG2 at 1400 K (Top); at 1700 K (Bottom)

Reaction Pathway Analysis

Similar to the 20 atm condition, the reaction path analysis was carried out for mixture 2 at 50 atm for natural gas oxidation in order to understand the important reaction pathways involved in CO formation. The UCF 2022 reaction mechanism was again used for this analysis.

The initiation of methane combustion in a natural gas oxidation mixture at 50 atm is very similar to the 20 atm condition. It begins in the same manner, following reactions R4-R5 to branch and form both CH_2 and CH_2O from the methyl radical obtained from the initial methane decomposition. In the first branch, CH_2O will form HCO which will continue on to either form CO_2 (the same pathway as the 20 atm condition, reactions R6, R7, R10) or CO directly via the same hydrogen abstraction and third body interactions as before (R8, R9). The second branch will see CH_2 behaving in a similar matter to the 20 atm condition, following reactions R11 and R12 to form CO_2 and HCO but now with an additional pathway to directly form CO by reacting with oxygen (R35). The pathway terminates in the same manner, with CO_2 forming CO via reactions R13 and R14. The new reaction is listed in Table 8 and the reaction/decomposition pathways can be seen in Figure 29.

Table 8: Reactions for 1400 K, 50 atm, CH_4 decomposition of NG2

R35	CH2+O2 = CO+OH+H

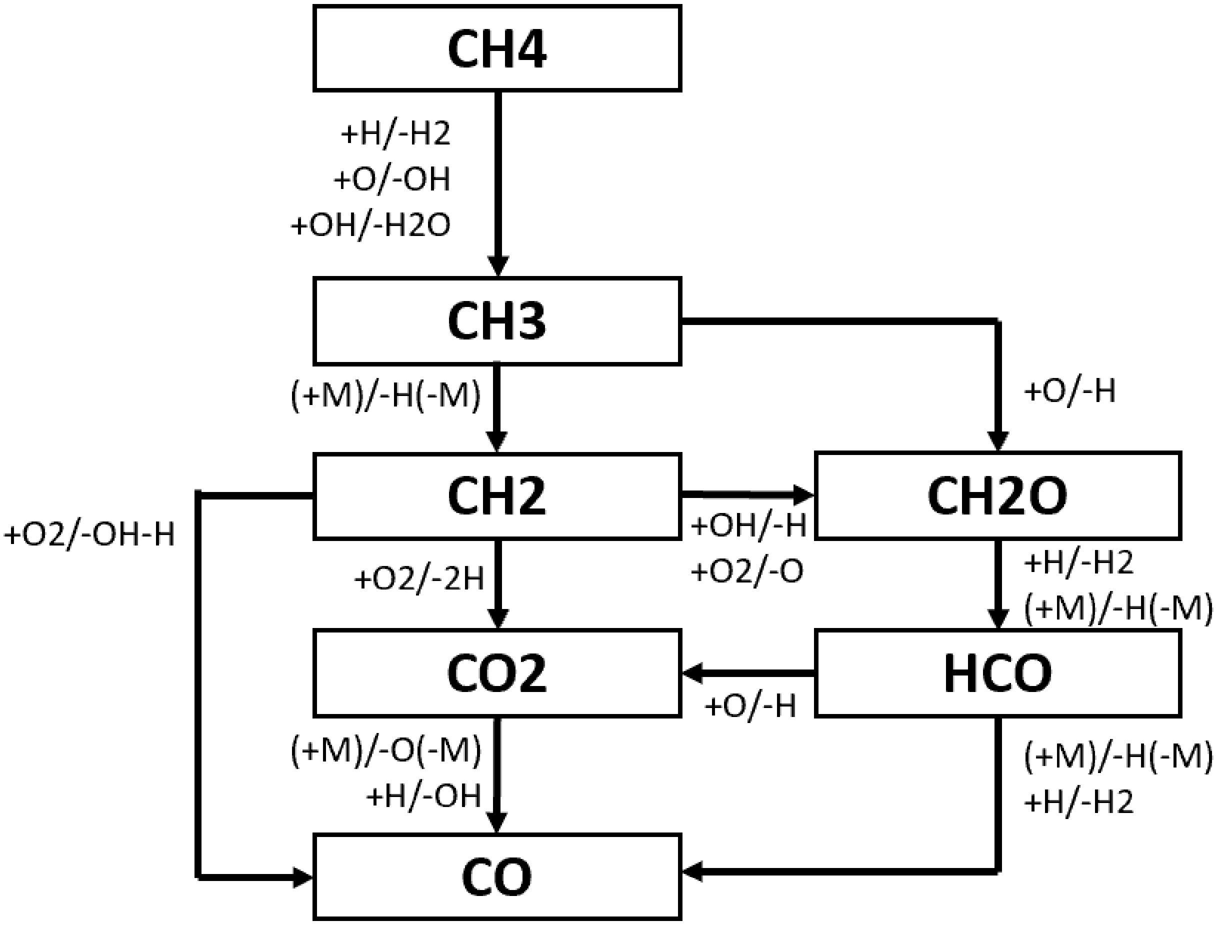

Figure 29: Major reaction pathways to CO for 1400 K, 50 atm, CH_4 decomposition of NG2

High Pressure Natural Gas Blends

Ignition Delay Times

Shock tube ignition delay times of various blends of natural gas at 100 atm are now offered to compare the effect of methane purity on LNG fuels. The experimental data with best fit lines can be seen in Figure 30. Again, the obvious trend of elevated temperature resulting in quicker IDT for every mixture is confirmed. It was also found that, when comparing various blends of natural gas, higher CH_4 purity levels generally result in an increase in ignition delay time. However, as was apparent in the 50 atm case where NG2, NG3, and NG4 were within the margin of error throughout the temperature range, for this 100 atm case, NG1, NG2, NG3, and NG4 are all now much closer in value. Even NG1 which had remained outside the margin of error in the 50 atm experiments is now within the margin of error of NG2 throughout the temperature range. This is again indicating that at higher pressures, the methane purity in the natural gas blends does not have as large an effect as at the lower pressure conditions.

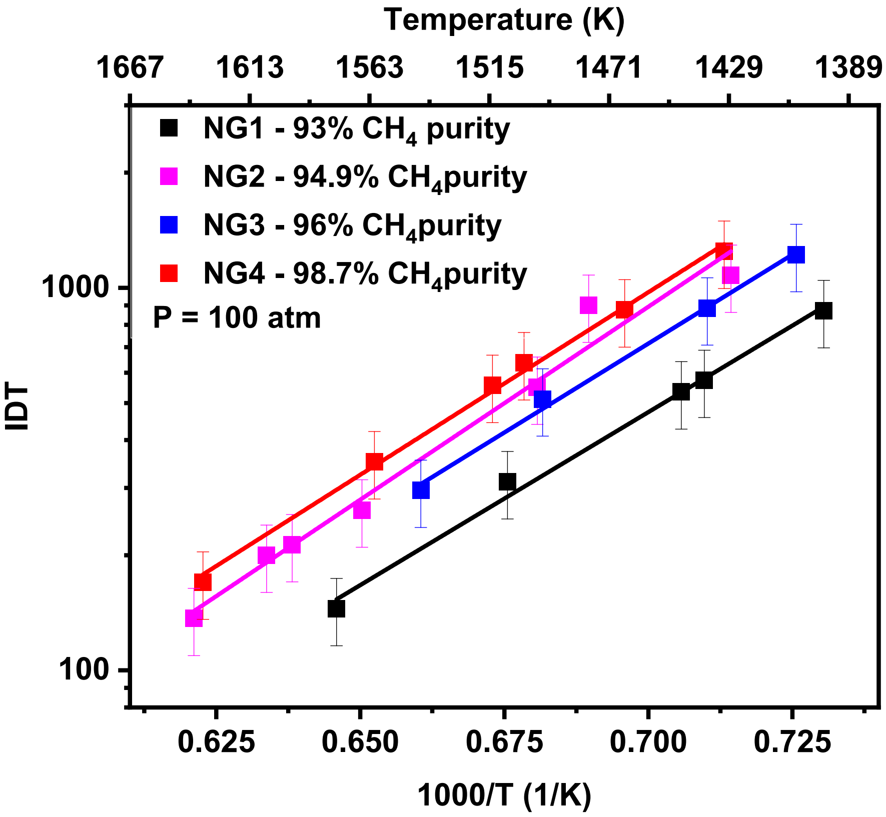

Figure 30: Comparison of shock tube IDTs during NG oxidation at 100 atm with best fit lines

Figure 31 shows the model comparison for all neat NG mixtures at 100 atm with the UCF 2022 mechanism shown in blue and the GRI 3.0 mechanism in red. The 100 atm condition varies slightly from the trend seen in the 50 atm condition (where it was seen that for mixtures NG2, NG3, and NG4, the mechanism overpredicted the IDTs outside the margin of error). Instead of overpredicting for NG1, NG2, NG3, and NG4, the 100 atm condition is largely able to capture the experimental behavior for all of the mixtures. The GRI 3.0 mechanism underpredicts the IDTs for each case. This could indicate that the mechanism could use further development for intermediate pressures since it performed well at the low pressure 20 atm and the high pressure 100 atm conditions.

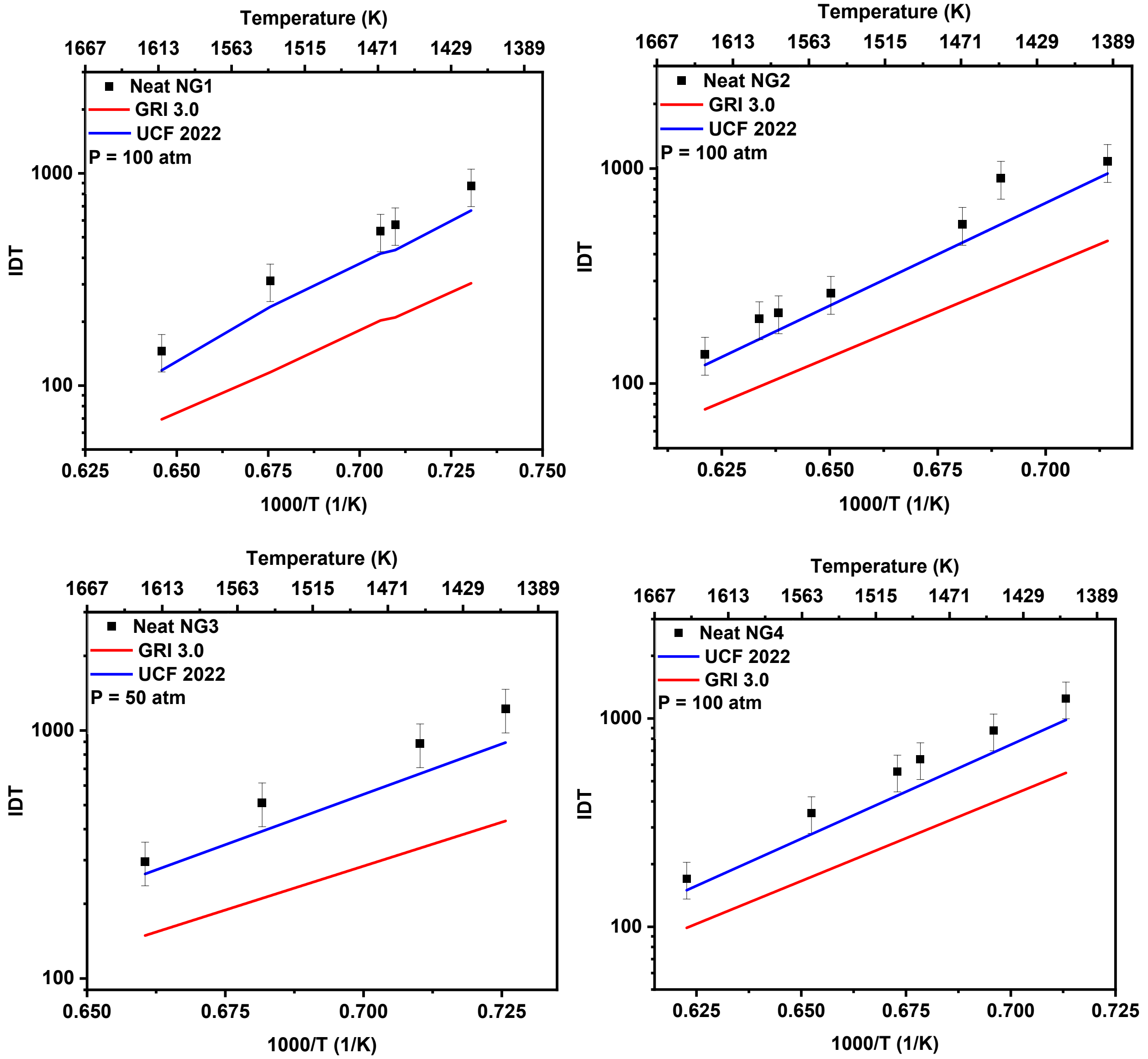

Figure 31: Comparison of 100 atm experimental IDTs and models during oxidation of NG1 (Top Left); NG2 (Top Right); NG3 (Bottom Left); NG4 (Bottom Right)

Sensitivity Analysis

The UCF 2022 mechanism is used again for the 100 atm sensitivity analysis, and the analysis was carried out in the same way as described in the low-pressure sensitivity analysis section. Again, trends in the sensitivity studies hold true for all NG mixtures and, as such, only NG2 will be shown.

Similar to both the 20 and 50 atm condition, when comparing the NG2 mixtures for the low and high temperature cases, the scales of the reactions are very different. While the top reactions are similar, the $2CH_3$=>C_2H_6 reaction goes from a sensitivity coefficient of 21.1 at 1400 K to a sensitivity coefficient of 1.45 at 1700 K showing a large dependence on temperature. Comparing this 100 atm pressure case to both of the lower pressure conditions, it can be seen that, again, most of the higher-pressure reactions are less sensitive in comparison to their lower pressure counterparts. This aligns with the results seen in the IDTs, indicating that, at high pressures, the effect of methane purity in natural gas blends is not as prevalent as it is at lower pressures. The sensitivity results can be seen in Figure 32.

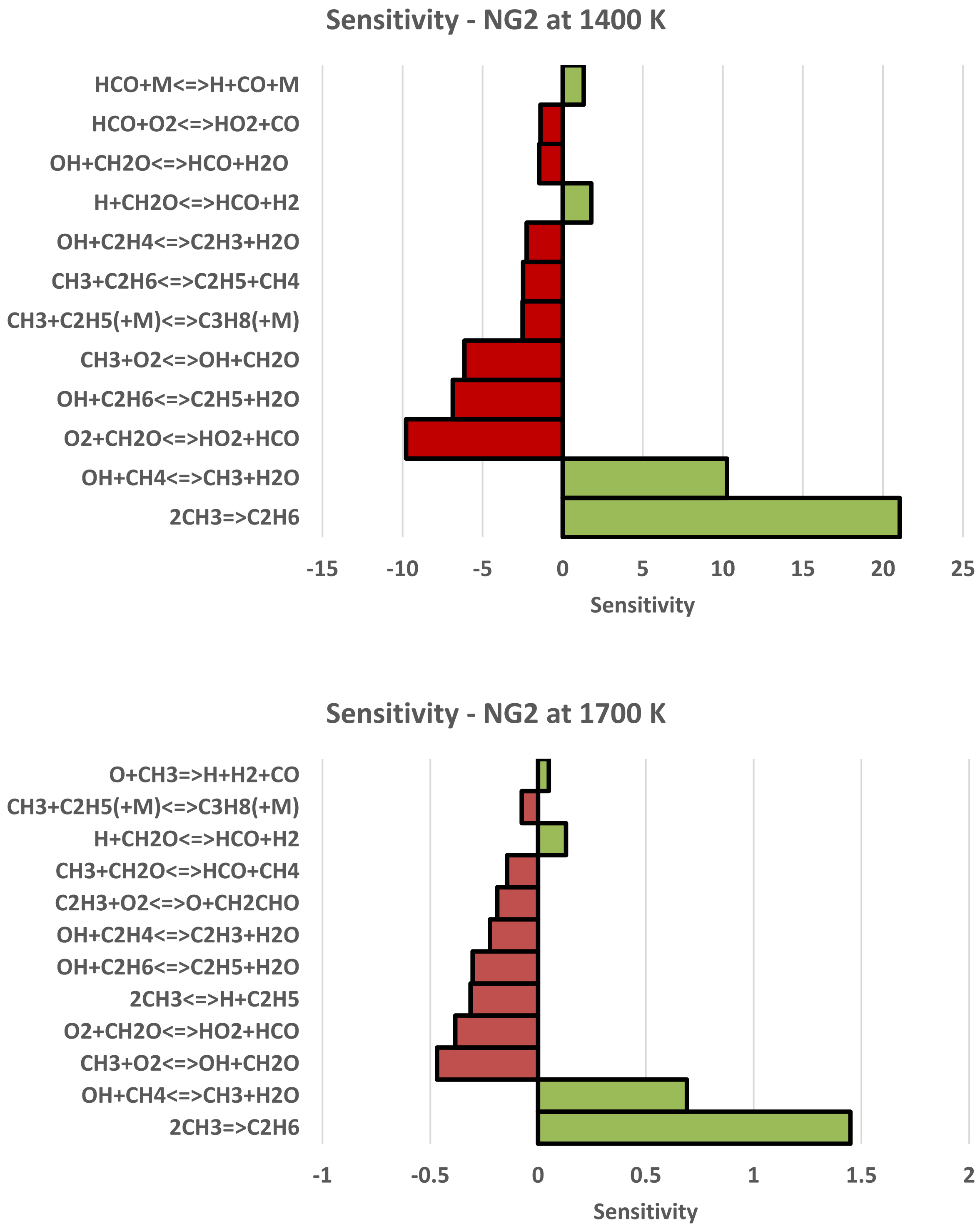

Figure 32: IDT Sensitivity analysis at 100 atm for NG2 K (Top); at 1700 K (Bottom)

Reaction Pathway Analysis

The reaction path analysis was also carried out for mixture 2 at 100 atm for natural gas oxidation in order to understand the important reaction pathways involved in CO formation. The UCF 2022 reaction mechanism was utilized for this analysis.

The initiation of methane combustion in a natural gas oxidation mixture at 100 atm is similar to the 20 and 50 atm conditions. It begins in the same manner, following reactions R1-R3 to form the initial methyl radical groups. From CH_3, the main reaction path includes the methyl radical reacting with HCO to release a hydrogen-atom radical and form CH_2CO (R36). From CH_2CO, there are three branching pathways. The first is the formation of HCO from CH_2CO oxygen abstraction or by reacting with OH (R37, R38). From here, the reaction pathway mirrors that of the previous pressure conditions, with HCO forming CO2 and then terminating in CO formation (R10, R13, R14). In the next branch, CH_2CO will form HCCO either from hydrogen abstraction or by reacting with the O-atom radical (R39, R40). This reaction path will then terminate in CO either via reactions with the O or H-atom radicals or third body interactions (R41-R43). The final branch shows CH_2CO directly forming CO by a third body interaction as well as by reacting with a hydrogen-atom radical, releasing a methyl group as well as CO (R44, R45). The new reactions are listed in Table 9 and the reaction/decomposition pathways can be seen in Figure 33.

Table 9: Reactions for 1400 K, 100 atm, CH_4 decomposition of NG2

R36	CH3+HCO = CH2CO+H	**R41**	HCCO+O = CO+H
R37	CH2CO+OH = HCO+H	**R42**	HCCO+H = CO+CH2
R38	CH2CO+O2 = HCO+O	**R43**	HCCO(+M) = CO+CH(+M)
R39	CH2CO+H = HCCO+H2	**R44**	CH2CO+H = CO+CH3
R40	CH2CO+O = HCOO+OH	**R45**	CH2CO(+M) = CO+CH2(+M)

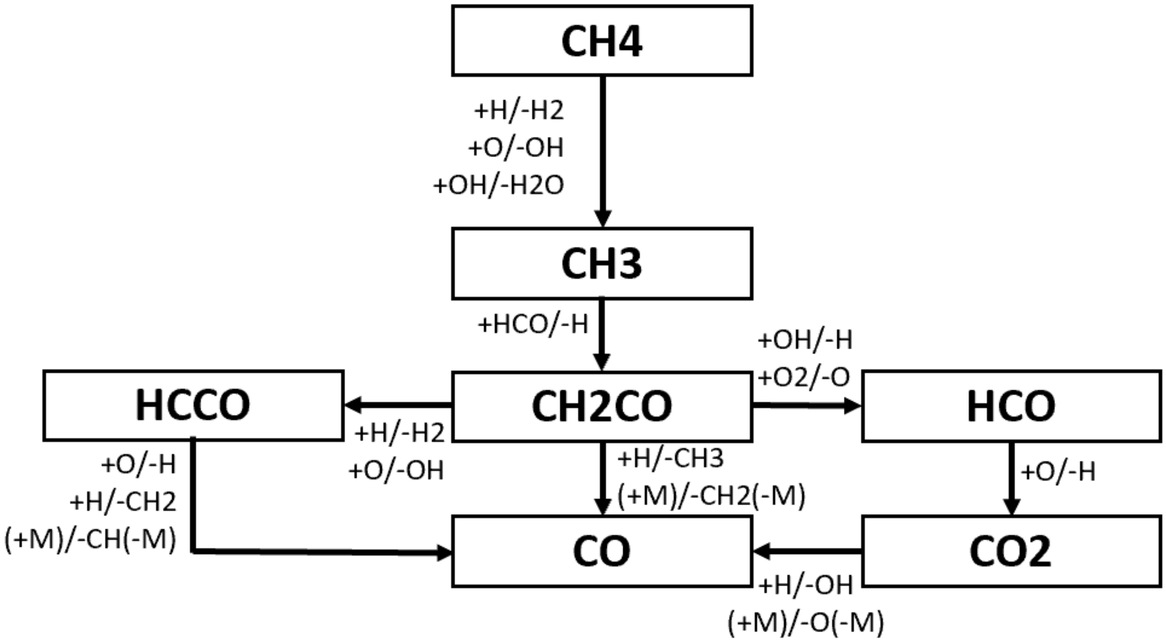

Figure 33: Major reaction pathways to CO for 1400 K, 100 atm, CH_4 decomposition of NG2

Chemiluminescent Imaging

CH* chemiluminescent image processing was performed on the videos taken during hot fire tests at MSFC as discussed in Chapter 2. Post-processing included removal of background noise through subtracting time-averaged videos taken of similar weather conditions before each test as well as basic filtering/LUT adjustments and normalization. Pseudo-color processing was also added for ease of visualization. These images offer insight into the combustion process and are largely presented as a showcase of the opportunity for further work such as direct comparison with CFD simulations performed with the UCF 2022 mechanism. Figure 34 shows a high temperature and low temperature hot fire test, both at an average pressure of 50 atm.

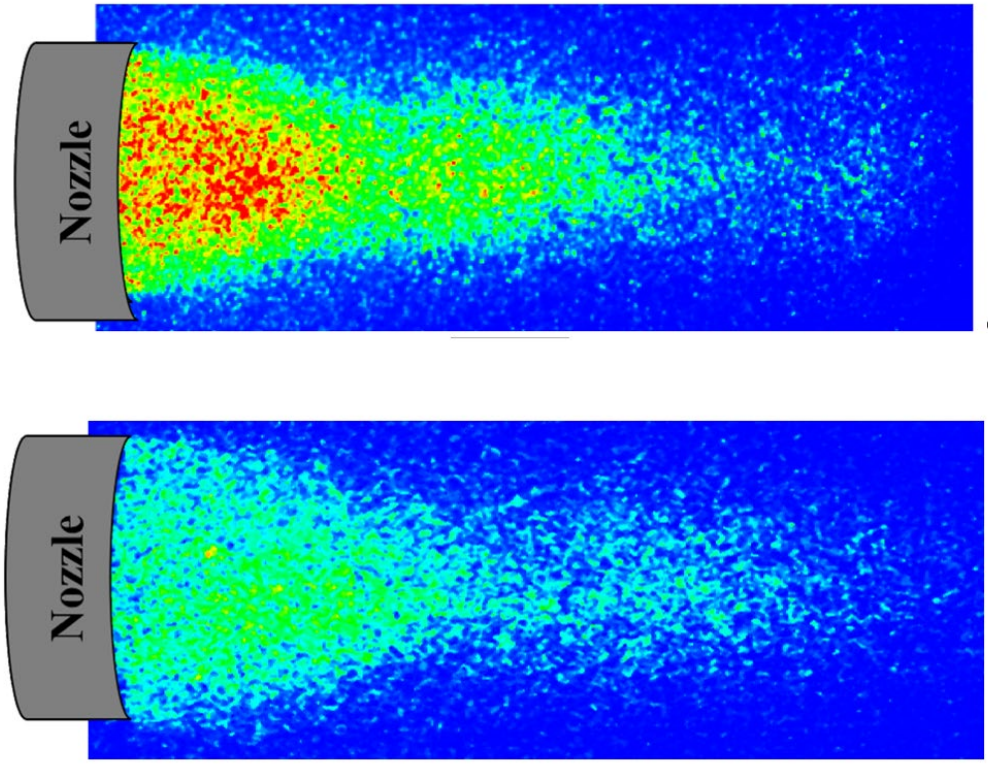

Figure 34: CH*chemiluminescent images at high temperature (Top); Low temperature (Bottom)

CHAPTER FIVE: CONCLUSIONS AND FUTURE WORK

Shock tube experiments were conducted to study the oxidation of four different natural gas blends at an equivalence ratio of 1 and were run at pressures of 20, 50, and 100 atm over temperatures ranging from 1400 to 1700 K. The 20 atm experiments featured each of the four natural gas blends with N_2O addition to model the effects of nitrogen-carriers on natural gas blends as well as additional experiments run at equivalence ratios of 0.5 and 2. CO time histories were obtained for the 20 atm test campaign and ignition delay times were measured for all pressures. Experimental results were compared to the UCF 2022 and GRI 3.0 chemical kinetic mechanisms to identify discrepancies between experimental data and modeling predictions and further improve the mechanism to provide more accurate modeling of natural gas fuels for rocket engine applications.

Results from the 20 bar experiments demonstrated that the methane-purity level had a large effect on IDTs, with the IDT for NG4 doubling that of NG1 in the low temperature range. It was also determined that the UCF 2022 mechanism was largely able to capture the experimental behavior of each of the natural gas blends throughout the entire temperature range. For N2O addition to the natural gas blends, it was found that the higher the methane purity, the larger the effect N2O had on IDT. For example, NG1 (93% CH4 purity) had minimal variance between neat and N2O addition, while NG4 (98.7% CH4 purity) had faster IDTs with N2O addition, outside of the margin of error. For the equivalence ratio, it was apparent that increasing the equivalence ratio resulted in an increase in IDT due to the increased amount of high hydrocarbons. The UCF 2022 model was able to capture the ignition behavior with N2O addition and the 0.5 and 2.0 equivalence ratios, as well. For CO formation, it was found that the higher the CH4 concentration/purity, the longer it takes CO to form and less CO will form within the test time. For the N2O addition cases, there was little difference in CO production as compared to the neat mixtures due to the low amount of N2O added. The UCF 2022 model well captured the initial formation of CO for both sets of mixtures with variations in the peak value once formation rate increases. A sensitivity analysis and reaction path analysis were conducted and important reactions involved in the oxidation of natural gas were identified.

50 bar and 100 bar experiments also featured IDT measurements, with the difference in IDT between methane-purity blends decreasing as the pressure increased. The model began to show slight variations in model performance, but was able to capture experimental behavior just within the margin of error. Again, a sensitivity analysis and reaction path analysis were conducted and the important reactions involved were identified.

The current work explores various blends of natural gas/methane fuel with various impurities, including higher hydrocarbons as well as nitrogen-carriers and provides critical data necessary for further development and application of LNG fuels in rocket engines.

Future Work

Additionally, validation is still needed at even higher pressures (up to 600 atm) where few studies of this nature exist. To fully understand the ignition behavior of LNG rocket fuels, ignition studies and species time histories would be beneficial at these extreme pressures, including further refinement of the chemical kinetic model using these high pressure data points. Further analysis could also be done focusing on TDK modeling. Using a brute-force method to further reduce and refine the UCF 2022 mechanism's integration into the current TDK mechanism would result in a more accurate tool for use in CFD simulations during the design stages of engine development. CFD simulations using this reduced mechanism would be beneficial as they would provide model validation targets as well as validation for the experimental work via direct comparison to the experimental hot-fire images.

LIST OF REFERENCES

[1] 2022, "SPACE: The Dawn of a New Age," https://www.citigroup.com/global/insights/citigps/space_20220509.

[2] Rufford, T. E., Smart, S., Watson, G. C., Graham, B., Boxall, J., Da Costa, J. D., and May, E., 2012, "The removal of CO2 and N2 from natural gas: A review of conventional and emerging process technologies," Journal of Petroleum Science and Engineering, 94, pp. 123-154.

[3] 2007, "PERFORMANCE SPECIFICATION: PROPELLANT, METHANE ", D. o. Defense, ed., Department of Defense.

[4] 2003, "Natural Gas Specs Sheet," North American Energy Standards Board.

[5] Nickerson, G., Coats, D., and Bartz, J., 1973, "The two-dimensional kinetic (TDK) reference computer program: engineering and programing manual."

[6] Nickerson, G. R., and Dang, L. D., 1983, "Improved Two-Dimensional Kinetics (TDK) computer program."

[7] Huang, J., Hill, P. G., Bushe, W. K., and Munshi, S. R., 2004, "Shock-tube study of methane ignition under engine-relevant conditions: experiments and modeling," Combustion and Flame, 136(1), pp. 25-42.

[8] Seery, D. J., and Bowman, C. T., 1970, "An experimental and analytical study of methane oxidation behind shock waves," Combustion and Flame, 14(1), pp. 37-47.

[9] Skinner, G. B., and Ruehrwein, R. A., 1959, "Shock tube studies on the pyrolysis and oxidation of methane," The Journal of Physical Chemistry, 63(10), pp. 1736-1742.

[10] Cheng, R. K., and Oppenheim, A. K., 1984, "Autoignition in methane–hydrogen mixtures," Combustion and Flame, 58(2), pp. 125-139.

[11] Petersen, E. L., Kalitan, D. M., Simmons, S., Bourque, G., Curran, H. J., and Simmie, J. M., 2007, "Methane/propane oxidation at high pressures: Experimental and detailed chemical kinetic modeling," Proceedings of the Combustion Institute, 31(1), pp. 447-454.

[12] Dagaut, P., and Dayma, G., 2006, "Hydrogen-enriched natural gas blend oxidation under high-pressure conditions: Experimental and detailed chemical kinetic modeling," International Journal of Hydrogen Energy, 31(4), pp. 505-515.

[13] Petersen, E. L., Hall, J. M., Smith, S. D., de Vries, J., Amadio, A. R., and Crofton, M. W., 2007, "Ignition of Lean Methane-Based Fuel Blends at Gas Turbine Pressures," Journal of Engineering for Gas Turbines and Power, 129(4), pp. 937-944.

[14] Koroglu, B., Pryor, O. M., Lopez, J., Nash, L., and Vasu, S. S., 2016, "Shock tube ignition delay times and methane time-histories measurements during excess CO2 diluted oxy-methane combustion," Combustion and Flame, 164, pp. 152-163.

[15] Eubank, C. S., Rabinowitz, M. J., Gardiner, W. C., and Zellner, R. E., 1981, "Shock-initiated ignition of natural gas—Air mixtures," Symposium (International) on Combustion, 18(1), pp. 1767-1774.

[16] Shao, J., Ferris, A. M., Choudhary, R., Cassady, S. J., Davidson, D. F., and Hanson, R. K., 2020, "Shock-induced ignition and pyrolysis of high-pressure methane and natural gas mixtures," Combustion and Flame, 221, pp. 364-370.

[17] Karimi, M., Ochs, B., Liu, Z., Ranjan, D., and Sun, W., 2019, "Measurement of methane autoignition delays in carbon dioxide and argon diluents at high pressure conditions," Combustion and Flame, 204, pp. 304-319.

[18] Petersen, E. L., Davidson, D. F., and Hanson, R. K., 1999, "Kinetics modeling of shock-induced ignition in low-dilution CH4/O2 mixtures at high pressures and intermediate temperatures," Combustion and Flame, 117(1), pp. 272-290.

[19] Petersen, E. L., Röhrig, M., Davidson, D. F., Hanson, R. K., and Bowman, C. T., 1996, "High-pressure methane oxidation behind reflected shock waves," Symposium (International) on Combustion, 26(1), pp. 799-806.

[20] Petersen, E. L., Davidson, D. F., and Hanson, R. K., 1999, "Ignition delay times of Ram accelerator CH/O/diluent mixtures," Journal of Propulsion and Power, 15(1), pp. 82-91.

[21] Higgin, R. M. R., and Williams, A., 1969, "A shock-tube investigation of the ignition of lean methane and n-butane mixtures with oxygen," Symposium (International) on Combustion, 12(1), pp. 579-590.

[22] Morimoto, S. S., Kawabata, Y., Sakurai, T., and Amano, T., 2001, "Operating characteristics of a natural gas-fired homogeneous charge compression ignition engine (performance improvement using EGR)," No. 0148-7191, SAE Technical Paper.

[23] Naber, J. D., Siebers, D. L., Westbrook, C. K., Caton, J. A., and Di Julio, S. S., 1994, "Natural gas autoignition under diesel conditions: experiments and chemical kinetic modeling," SAE transactions, pp. 1735-1753.

[24] Li, M., Wu, H., Zhang, T., Shen, B., Zhang, Q., and Li, Z., 2020, "A comprehensive review of pilot ignited high pressure direct injection natural gas engines: Factors affecting combustion, emissions and performance," Renewable and Sustainable Energy Reviews, 119, p. 109653.

[25] Naber, J., Siebers, D., Di Julio, S., and Westbrook, C., 1994, "Effects of natural gas composition on ignition delay under diesel conditions," Combustion and Flame, 99(2), pp. 192-200.

[26] Khosravi, M., Rochussen, J., Yeo, J., Kirchen, P., McTaggart-Cowan, G., and Wu, N., "Effect of Fuelling Control Parameters on Combustion Characteristics of Diesel-Ignited Natural Gas Dual-Fuel Combustion in an Optical Engine," Proc. ASME 2016 Internal Combustion Engine Division Fall Technical ConferenceV001T03A012.

[27] Komarov, I., Kharlamova, D., Makhmutov, B., Shabalova, S., and Kaplanovich, I., 2020, "Natural Gas-Oxygen Combustion in a Super-Critical Carbon Dioxide Gas Turbine Combustor," E3S Web Conf., 178, p. 01027.

[28] McTaggart-Cowan, G., Mann, K., Huang, J., Singh, A., Patychuk, B., Zheng, Z. X., and Munshi, S., 2015, "Direct Injection of Natural Gas at up to 600 Bar in a Pilot-Ignited Heavy-Duty Engine," SAE International Journal of Engines, 8(3), pp. 981-996.

[29] Hargis, J. W., and Petersen, E. L., 2015, "Methane Ignition in a Shock Tube with High Levels of CO2 Dilution: Consideration of the Reflected-Shock Bifurcation," Energy & Fuels, 29(11), pp. 7712-7726.

[30] Donohoe, N., Heufer, A., Metcalfe, W. K., Curran, H. J., Davis, M. L., Mathieu, O., Plichta, D., Morones, A., Petersen, E. L., and Güthe, F., 2014, "Ignition delay times, laminar flame speeds, and mechanism validation for natural gas/hydrogen blends at elevated pressures," Combustion and Flame, 161(6), pp. 1432-1443.

[31] Frenklach, M., and Bornside, D. E., 1984, "Shock-initiated ignition in methane-propane mixtures," Combustion and Flame, 56(1), pp. 1-27.

[32] Krishnan, K. S., Ravikumar, R., and Bhaskaran, K. A., 1983, "Experimental and analytical studies on the ignition of methane□acetylene mixtures," Combustion and Flame, 49(1), pp. 41-50.

[33] Lifshitz, A., Scheller, K., Burcat, A., and Skinner, G. B., 1971, "Shock-tube investigation of ignition in methane-oxygen-argon mixtures," Combustion and Flame, 16(3), pp. 311-321.

[34] Crossley, R. W., Dorko, E. A., Scheller, K., and Burcat, A., 1972, "The effect of higher alkanes on the ignition of methane-oxygen-argon mixtures in shock waves," Combustion and Flame, 19(3), pp. 373-378.

[35] Vallabhuni, S. K., Lele, A. D., Patel, V., Lucassen, A., Moshammer, K., AlAbbad, M., Farooq, A., and Fernandes, R. X., 2018, "Autoignition studies of Liquefied Natural Gas (LNG) in a shock tube and a rapid compression machine," Fuel, 232, pp. 423-430.

[36] Crane, J., Shi, X., Xu, R., and Wang, H., 2022, "Natural gas versus methane: Ignition kinetics and detonation limit behavior in small tubes," Combustion and Flame, 237, p. 111719.

[37] Mehta, J. M., 2022, "A Study of Conventional Fuels for Unconventional Applications,"Ph.D., University of Illinois at Chicago, United States -- Illinois.

[38] Sahu, A. B., Mohamed, A. A. E.-S., Panigrahy, S., Bourque, G., and Curran, H., 2021, "Ignition Studies of C1–C7 Natural Gas Blends at Gas-Turbine-Relevant Conditions," Journal of Engineering for Gas Turbines and Power, 143(8).

[39] Grillo, A., and Slack, M. W., 1976, "Shock tube study of ignition delay times in methane□oxygen□nitrogen□argon mixtures," Combustion and Flame, 27, pp. 377-381.

[40] Oh, S., Park, C., Kim, S., Kim, Y., Choi, Y., and Kim, C., 2021, "Natural gas–ammonia dual-fuel combustion in spark-ignited engine with various air–fuel ratios and split ratios of ammonia under part load condition," Fuel, 290, p. 120095.

[41] Zhao, L., Cao, M., Xu, D., Wang, X., Gutierrez, J., Sosa, S., and Tsotsis, T., 2020, "Pollutant Formation during Utilization of Renewable Natural Gas Containing Trace Ammonia Impurities," Industrial & Engineering Chemistry Research, 59(43), pp. 19177-19184.

[42] Mei, B., Ma, S., Zhang, Y., Zhang, X., Li, W., and Li, Y., 2020, "Exploration on laminar flame propagation of ammonia and syngas mixtures up to 10 atm," Combustion and Flame, 220, pp. 368-377.

[43] Okafor, E. C., Somarathne, K. D. K. A., Ratthanan, R., Hayakawa, A., Kudo, T., Kurata, O., Iki, N., Tsujimura, T., Furutani, H., and Kobayashi, H., 2020, "Control of NOx and other emissions in micro gas turbine combustors fuelled with mixtures of methane and ammonia," Combustion and Flame, 211, pp. 406-416.

[44] Deng, F., Yang, F., Zhang, P., Pan, Y., Zhang, Y., and Huang, Z., 2016, "Ignition Delay Time and Chemical Kinetic Study of Methane and Nitrous Oxide Mixtures at High Temperatures," Energy & Fuels, 30(2), pp. 1415-1427.

[45] Mével, R., and Shepherd, J. E., 2015, "Ignition delay-time behind reflected shock waves of small hydrocarbons–nitrous oxide(–oxygen) mixtures," Shock Waves, 25(3), pp. 217-229.

[46] Newman-Lehman, T., Grana, R., Seshadri, K., and Williams, F., 2013, "The structure and extinction of nonpremixed methane/nitrous oxide and ethane/nitrous oxide flames," Proceedings of the Combustion Institute, 34(2), pp. 2147-2153.

[47] Zabarnick, S., 1992, "A Comparison of CH4/NO/02 and CH4/N20 Flames by LIF Diagnostics and Chemical Kinetic Modeling," Combustion Science and Technology, 83(1-3), pp. 115-134.

[48] Rahman, R. K., Barak, S., Ninnemann, E., Hosangadi, A., Zambon, A., and Vasu, S. S., 2020, "Probing the effects of NOx and SOx impurities on oxy-fuel combustion in supercritical CO2: Shock tube experiments and chemical kinetic modeling," Journal of Energy Resources Technology, 142(12).

[49] Mathieu, O., Pemelton, J. M., Bourque, G., and Petersen, E. L., 2015, "Shock-induced ignition of methane sensitized by NO2 and N2O," Combustion and Flame, 162(8), pp. 3053-3070.

[50] An, B., Wang, Z., and Sun, M., 2021, "Ignition dynamics and combustion mode transitions in a rocket-based combined cycle combustor operating in the ramjet/scramjet mode," Aerospace Science and Technology, 118, p. 106951.

[51] Hong, J., Levin, D., Collins, R., Emery, J., Tietjen, A., Hong, J., Levin, D., Collins, R., Emery, J., and Tietjen, A., "Comparison of Atlas ground based plume imagery with chemically reacting flow solutions," 32nd Thermophysics Conference.

[52] Toscano, A. M., Lato, M. R., Fontanarosa, D., and De Giorgi, M. G., 2022, "Optical diagnostics for solid rocket plumes characterization: A review," Energies, 15(4), p. 1470.

[53] Chandler, A. A., 2012, An investigation of liquefying hybrid rocket fuels with applications to solar system exploration, Stanford University.

[54] Jens, E. T., Miller, V. A., and Cantwell, B. J., 2016, "Schlieren and OH* chemiluminescence imaging of combustion in a turbulent boundary layer over a solid fuel," Experiments in Fluids, 57(3), p. 39.

[55] Chandler, A., Jens, E., Cantwell, B., and Hubbard, G. S., "Visualization of the liquid layer combustion of paraffin fuel for hybrid rocket applications," Proc. 48th AIAA/ASME/SAE/ASEE Joint Propulsion Conference & Exhibit, p. 3961.

[56] Avital, G., Cohen, Y., Gamss, L., Kanelbaum, Y., Macales, J., Trieman, B., Yaniv, S., Lev, M., Stricker, J., and Sternlieb, A., 2001, "Experimental and computational study of infrared emission from underexpanded rocket exhaust plumes," Journal of thermophysics and heat transfer, 15(4), pp. 377-383.

[57] Qinglin, N., Zhihong, H., and Shikui, D., 2017, "IR radiation characteristics of rocket exhaust plumes under varying motor operating conditions," Chinese Journal of Aeronautics, 30(3), pp. 1101-1114.

[58] Liu, Y., Tan, J., Gao, Z., Wang, T., and Wan, M., 2021, "Experimental investigation of chemiluminescence and NOx emission characteristics in a lean premixed dual-swirl flame," Case Studies in Thermal Engineering, 28, p. 101653.

[59] Cho, K. Y., Codoni, J. R., Rankin, B. A., Hoke, J., and Schauer, F., "High-repetition-rate chemiluminescence imaging of a rotating detonation engine," Proc. 54th AIAA aerospace sciences meeting, p. 1648.

[60] Rankin, B. A., Richardson, D. R., Caswell, A. W., Naples, A., Hoke, J., and Schauer, F., "Imaging of OH* chemiluminescence in an optically accessible nonpremixed rotating detonation engine," Proc. 53rd AIAA aerospace sciences meeting, p. 1604.

[61] Rothman, L. S., Gordon, I. E., Babikov, Y., Barbe, A., Chris Benner, D., Bernath, P. F., Birk, M., Bizzocchi, L., Boudon, V., Brown, L. R., Campargue, A., Chance, K., Cohen, E. A., Coudert, L. H., Devi, V. M., Drouin, B. J., Fayt, A., Flaud, J. M., Gamache, R. R., Harrison, J. J., Hartmann, J. M., Hill, C., Hodges, J. T., Jacquemart, D., Jolly, A., Lamouroux, J., Le Roy, R. J., Li, G., Long, D. A., Lyulin, O. M., Mackie, C. J., Massie, S. T., Mikhailenko, S., Müller, H. S. P., Naumenko, O. V., Nikitin, A. V., Orphal, J., Perevalov, V., Perrin, A., Polovtseva, E. R., Richard, C., Smith, M. A. H., Starikova, E., Sung, K., Tashkun, S., Tennyson, J., Toon, G. C.,

Tyuterev, V. G., and Wagner, G., 2013, "The HITRAN2012 molecular spectroscopic database," Journal of Quantitative Spectroscopy and Radiative Transfer, 130, pp. 4-50.

[62] Ninnemann, E., Kim, G., Laich, A., Almansour, B., Terracciano, A. C., Park, S., Thurmond, K., Neupane, S., Wagnon, S., Pitz, W. J., and Vasu, S. S., 2019, "Co-optima fuels combustion: A comprehensive experimental investigation of prenol isomers," Fuel, 254, p. 115630.

[63] Urso, J., 2020, "A Shock Tube and Diagnostics for Surface Effects at Elevated Pressures with Applications to Methane/Ammonia Ignition," Electronic Theses and Dissertations.

[64] Laich, A. R., Ninnemann, E., Neupane, S., Rahman, R., Barak, S., Pitz, W. J., Goldsborough, S. S., and Vasu, S. S., 2020, "High-pressure shock tube study of ethanol oxidation: Ignition delay time and CO time-history measurements," Combustion and Flame, 212, pp. 486-499.

[65] Tinker, D. C., Fedotowsky, T., Bardsley, R. A., and Gradl, P. R., "Development of Large-Scale Thrust Chambers using Laser Powder Directed Energy Deposition," AIAA SCITECH 2024 Forum.

[66] Fedotowsky, T., Williams, B., Gradl, P. R., and Tinker, D. C., "AL6061-RAM2 Development and Hot-Fire Testing using Additive Manufacturing Laser Powder Directed Energy Deposition for Liquid Rocket Engine Channel-Cooled Nozzles," AIAA SCITECH 2024 Forum.

[67] 2011, "CHEMKIN-PRO," R. Design, ed.San Diego, CA.

[68] Baker, J. B., Ramees K. Rahman, Michael Pierro, Jacklyn Higgs, Justin Urso, Cory Kinney, Subith Vasu, 2022, "AUTOIGNITION DELAY TIME MEASUREMENTS AND CHEMICAL KINETIC MODELING OF HYDROGEN/AMMONIA/NATURAL GAS MIXTURES," ASME J. Energy Resour Technol.

[69] Gregory P. Smith, D. M. G., Michael Frenklach, Nigel W. Moriarty, Boris Eiteneer, Mikhail Goldenberg, C. Thomas Bowman, Ronald K. Hanson, Soonho Song, William C. Gardiner, Jr., Vitali V. Lissianski, and Zhiwei Qin, "GRI 3.0," http://www.me.berkeley.edu/gri_mech/.

[70] Rahman, R. K., Barak, S., Manikantachari, K. R. V., Ninnemann, E., Hosangadi, A., Zambon, A., and Vasu, S. S., 2020, "Probing the Effects of NOx and SOx Impurities on Oxy-Fuel Combustion in Supercritical

CO2: Shock Tube Experiments and Chemical Kinetic Modeling," Journal of Energy Resources Technology, 142(12).

[71] Zhou, C.-W., Li, Y., Burke, U., Banyon, C., Somers, K. P., Ding, S., Khan, S., Hargis, J. W., Sikes, T., Mathieu, O., Petersen, E. L., AlAbbad, M., Farooq, A., Pan, Y., Zhang, Y., Huang, Z., Lopez, J., Loparo, Z., Vasu, S. S., and Curran, H. J., 2018, "An experimental and chemical kinetic modeling study of 1,3-butadiene combustion: Ignition delay time and laminar flame speed measurements," Combustion and Flame, 197, pp. 423-438.

[72] Baker, J. B., Rahman, R. K., Pierro, M., Higgs, J., Urso, J., Kinney, C., and Vasu, S., 2023, "Experimental ignition delay time measurements and chemical kinetics modeling of hydrogen/ammonia/natural gas fuels," Journal of Engineering for Gas Turbines and Power, 145(4), p. 041002.